Phosphate starvation-induced CORNICHON HOMOLOG 5 as endoplasmic reticulum cargo receptor for PHT1 transporters in *Arabidopsis*

Chang-Yi Chiu[1], Cheng-Da Tsai[1], Hui-Fang Lung[1], Jhih-Yi Wang[1], Ming-Hsuan Tsai[1], Alastair J. McGinness[2], Satomi Kanno[3], Verena Kriechbaumer,[2], Chiao-An Lu[1], Tzu-Yin Liu[1,4]

[1]Institute of Bioinformatics and Structural Biology, College of Life Sciences and Medicine, National Tsing Hua University, Hsinchu 30013, Taiwan.

[2]Endomembrane Structure and Function Research Group, School of Biological and Medical Sciences, Oxford Brookes University, Headington, Oxford OX3 0BP, UK

[3]Institute for Advanced Research, NAIAS, Nagoya University, Fro-cho, Chikusa-ku, Nagoya, Japan.

[4]Department of Life Science, College of Life Sciences and Medicine, National Tsing Hua University, Hsinchu 30013, Taiwan.

Corresponding author:

Tzu-Yin Liu

Email: tzliu@life.nthu.edu.tw

Short title: CNIH5 facilitates ER export of PHT1 transporters

Keywords: CORNICHON HOMOLOG (CNIH), ER cargo receptor, coat protein complex II (COPII), ER exit sites (ERES), phosphate starvation, phosphate transporter

Abstract

Inorganic phosphate (Pi) is essential for plant growth and is acquired and distributed by the plasma membrane PHOSPHATE TRANSPORTER 1 proteins (PHT1s). Enhancing the abundance of PHT1s at the cell surface thus ensures plant productivity and sustainable agriculture. CORNICHON HOMOLOG proteins (CNIHs) are conserved eukaryotic cargo receptors that mediate the selective endoplasmic reticulum (ER) export of membrane proteins. In this study, we identified the *Arabidopsis thaliana CNIH5* (*AtCNIH5*) as a Pi starvation-inducible gene, preferentially expressed in vascular tissues and outer root cell layers above the meristem. *At*CNIH5 co-localizes to the *At*SAR1A/*At*SEC16A/*At*SEC24A-labeled ER exit sites and interacts with *At*PHT1;1. Loss of *AtCNIH5* confers reduced shoot Pi levels under Pi sufficiency due to the reduced translocation of Pi from roots to shoots, as well as decreased Pi uptake under Pi deficiency. The *cnih5* mutant exhibits decreased abundance of *At*PHT1s but increased PHOSPHATE TRANSPORTER TRAFFIC FACILITATOR1 (*At*PHF1), which enables the ER exit of PHT1s. The *cnih5* mutant also shows a lower plasma membrane targeting efficiency of split-GFP tagged-*At*PHT1;1 in the root hair and the epidermis within the root transition/elongation zone. Consistently, dysfunctional *At*CNIH5 exerts a suppressive effect on the growth of *phf1* and alleviates Pi toxicity in the Pi overaccumulator *pho2*. However, the *in vivo* protein–protein interaction and degradation assays indicated that *At*CNIH5 is not a direct target of *At*PHO2. Our findings unveil that *At*CNIH5 is a low Pi-responsive ER cargo receptor that interplays with *At*PHF1 to promote the plasma membrane targeting of *At*PHT1s in a cell-type-dependent manner.

Introduction

Membrane trafficking that dictates the plasma membrane (PM) proteins in reaching their destination is intimately linked with plants' plasticity to changing environments and, thus, crucial for plant growth and fitness under adverse conditions. Among the endoplasmic reticulum (ER) accessory proteins involved in membrane trafficking, CORNICHON HOMOLOG (CNIH) proteins are responsible for the selective export of membrane cargoes to the Golgi or post-Golgi compartments by cycling between the ER and the Golgi (Powers & Barlowe, 1998, Harmel *et al.*, 2012). They are conserved in eukaryotes and presumably harbour three membrane-spanning α-helixes with the N-terminus towards the cytoplasm based on the "positive-inside rule" and supported by some experimental evidence (Powers & Barlowe, 2002). However, cryo-electron microscopy revealed that the N- and C-termini of mammalian CNIH2 and CNIH3 are located in the extracellular space (Nakagawa, 2019, Zhang *et al.*, 2021, Gangwar *et al.*, 2023). The AlphaFold model also predicts that the budding yeast *Saccharomyces cerevisiae Sc*CNIH/Erv14 has a topology of four transmembrane domains with both termini located in the ER lumen (Lagunas-Gomez *et al.*, 2023).

The *Drosophila* cornichon is the first identified CNIH that promotes the ER export of the transforming growth factor α (TGFα)-like growth factor and its trafficking towards the oocyte surface during oogenesis (Roth *et al.*, 1995, Bökel *et al.*, 2006). In yeast, systematic genetic manipulations combined with automated microscopy screening uncovered that Erv14 serves as an ER cargo receptor of about 40 membrane cargoes with diverse functions, including proteins involved in transport, budding, sporulation, and cell wall synthesis (Powers & Barlowe, 2002, Nakanishi *et al.*, 2007, Herzig *et al.*, 2012, Pagant *et al.*, 2015, Zimmermannová *et al.*, 2019, Powers & Barlowe, 1998). Of note, yeast cells lacking Erv14 showed normal PM localization of the K^+-importer Trk2 yet mistargeting its paralog Trk1, despite that Trk2 is nearly 55% identical to Trk1 (Zimmermannová *et al.*, 2019), suggesting a regulatory mechanism operating in the cargo selectivity of CNIHs. For instance, Erv14 employs multiple modes of cargo binding to meet the different requirements of various cargo proteins. It simultaneously binds to the membrane cargo and the coat protein complex II (COPII) subunit Sec24, thus incorporating the membrane cargo into the COPII carriers (Powers & Barlowe, 1998, Powers & Barlowe, 2002, Pagant *et al.*, 2015). Similarly, Sec24 was reported to recognize

81 two signals to efficiently drive the ER exit of client proteins, one on membrane cargoes
82 and the other on Erv14 (Pagant *et al.*, 2015).
83 Despite plant CNIH proteins (CNIHs) being less functionally characterized, they seem
84 to have a similar role to their yeast counterpart. The moss (*Physcomitrium patens*)
85 *Pp*CNIH2 was identified as a specific cargo receptor of the auxin efflux transporter
86 homolog PINA for its polar localization in protonema cells (Yáñez-Domínguez *et al.*,
87 2023). The rice (*Oryza sativa*) *Os*CNIH1 was shown to mediate the Golgi targeting of the
88 sodium transporter *Os*HKT1;3 (Rosas-Santiago *et al.*, 2015). Moreover, overexpression
89 of the pumpkin (*Cucurbita moschata* var. *Rifu*) *Cm*CNIH1 improves the salt tolerance by
90 regulating the PM localization of the sodium-selective transporter *Cm*HKT1;1 (Wei *et*
91 *al.*, 2023). The *Arabidopsis cnih1*, *cnih4*, and *cnih1/4* double mutants were shown to
92 exhibit reduced Ca^{2+} fluxes in the pollen tube tip due to the impaired targeting of
93 glutamate receptor-like channels (GLRs) (Wudick *et al.*, 2018). Furthermore, the patch-
94 clamp analysis of mammalian COS-7 cells expressing *At*GLR3.3 together with *At*CNIH1
95 and *At*CNIH4 displayed a current two-fold relative to those co-expressing *At*GLR3.3 with
96 *At*CNIH1 or *At*CNIH4 alone, indicating that the formation of *At*CNIH oligomers
97 potentially imposes an additional layer of regulation on cellular Ca^{2+} homeostasis
98 (Wudick *et al.*, 2018). Therefore, by modulating the trafficking of various transporters
99 along the secretory pathway, the plant CNIH family can regulate various ion homeostasis.
100 Phosphate (Pi) is known to be one of the most limiting mineral nutrients for plant growth
101 and productivity. Due to its chemical properties, Pi is primarily immobilized in the soil,
102 resulting in poor (Manning, 2008).bioavailability (Manning, 2008). To adapt to low Pi
103 availability, plants employ a series of strategies, including enhancing Pi acquisition
104 through the PM-localized PHOSPHATE TRANSPORTER 1 (PHT1) family (Poirier &
105 Bucher, 2002, Młodzińska & Zboińska, 2016). In *Arabidopsis*, *At*PHT1;1 and *At*PHT1;4
106 are responsible for up to 75% of Pi uptake under a wide range of Pi concentrations and
107 thus play dominant roles in Pi acquisition (Karthikeyan *et al.*, 2002, Mudge *et al.*, 2002,
108 Shin *et al.*, 2004, Ayadi *et al.*, 2015, Misson *et al.*, 2004). Under Pi sufficiency, *At*PHT1;1
109 also plays an important role in Pi translocation from roots to leaves (Ayadi *et al.*, 2015).
110 *At*PHT1;5 participates in Pi mobilization from source to sink organs (Nagarajan *et al.*,
111 2011). *At*PHT1;8 and *At*PHT1;9 contribute to both Pi uptake and Pi translocation toward
112 the vascular tissues in roots under Pi starvation (Remy *et al.*, 2012, Lapis-Gaza *et al.*,

113 2014).

114 Under Pi repletion, *AtPHT1;1* shows a robust gene expression in the root hair-
115 producing trichoblast and is the most abundant member (Mudge *et al.*, 2002, Karthikeyan
116 *et al.*, 2002, Ayadi *et al.*, 2015). In response to low Pi, *AtPHT1;1* is modestly induced,
117 mainly in the root epidermis, cortex, and root hair, and is detectable throughout the lateral
118 root cap (Mudge *et al.*, 2002, Karthikeyan *et al.*, 2002). *AtPHT1;4* is highly induced by
119 Pi limitation and expressed primarily in the epidermis, the cortex, and the root cap, but it
120 is also present at the lateral root branch points on the primary root and in the stele of
121 lateral roots (Misson *et al.*, 2004). Besides the low Pi induction of *PHT1* genes at the
122 transcriptional level, the trafficking of PHT1 proteins (PHT1s) to the PM is under
123 constant surveillance. The ER exit of PHT1s requires PHOSPHATE TRANSPORTER
124 TRAFFIC FACILITATOR1 (PHF1), an ER accessory protein sharing sequence
125 homology with the small GTPase SAR1 guanine nucleotide exchange factor (GEF)
126 SEC12 but missing the key catalytic residues required for the GEF activity (González *et*
127 *al.*, 2005). Dysfunction of *At*PHF1 specifically impairs Pi uptake by hampering the PM
128 targeting of PHT1s, leading to a reduced abundance of PHT1s at the PM and a lower
129 cellular Pi level, thereby activating Pi starvation-responsive (PSR) genes (González *et al.*,
130 2005, Bayle *et al.*, 2011). In rice, the phosphorylation status of the C-terminus of
131 *Os*PHT1s affects their interaction with *Os*PHF1, and thus the ER exit of *Os*PHT1s (Chen
132 *et al.*, 2015, Yang *et al.*, 2020). In addition, the turnover of PHT1s relies on the vacuolar
133 degradation mediated either by the ENDOSOMAL SORTING COMPLEXES
134 REQUIRED FOR TRANSPORT (ESCRT) III-related component (Cardona-López *et al.*,
135 2015) or the ubiquitin E2 conjugase PHOSPHATE2 (PHO2) and/or the ubiquitin E3
136 ligase NITROGEN LIMITATION ADAPTATION (NLA) (Lin *et al.*, 2013, Huang *et al.*,
137 2013, Park *et al.*, 2014). As a result, defective PHO2 or NLA confers Pi overaccumulation
138 in plants due to increased accumulation of PHT1s (Lin *et al.*, 2013, Huang *et al.*, 2013).

139 Previous transcriptome profiling has uncovered *AtCNIH5* as a Pi starvation-induced
140 gene with unknown implications (Müller *et al.*, 2007, Liu *et al.*, 2016). The membrane
141 proteomics analysis of *Arabidopsis pho2* roots also revealed a significant increase in
142 *At*CNIH5 (AT4G12090), along with a higher level of *At*PHT1;1–1;4 and *At*PHF1 (Huang
143 *et al.*, 2013). Although it remains to be determined whether *At*CNIH5 is a direct target of
144 *At*PHO2, when querying a yeast split-ubiquitin-based *Arabidopsis* interactome database

145 (*At*CNIH5 not included), we found that *At*CNIH1 interacts with *At*PHT1;9 and *At*PHF1
146 (Jones Alexander *et al.*, 2014). These data prompted us to speculate that Pi starvation-
147 induced *At*PHF1, *At*CNIH5, and *At*PHT1s are genetically and functionally linked. We
148 were thus curious whether *At*CNIH proteins (*At*CNIHs), particularly *At*CNIH5, are
149 involved in the regulatory mechanism for the post-ER trafficking of *At*PHT1s. In this
150 study, we characterized *AtCNIH5* as the sole *AtCNIH* gene induced by Pi starvation in
151 the outer root cell layers, including epidermal, cortical, and endodermal cells. We showed
152 that in agro-infiltrated *Nicotiana benthamiana* (*N. benthamiana*) leaves, the fluorescent-
153 tagged *At*CNIH5 is ER-localized and closely associated with the ER exit sites (ERES)
154 markers *At*SAR1A, *At*SEC16A, and *At*SEC24A. We confirmed the interaction of
155 *At*CNIH5 with *At*PHT1;1 using the *in-planta* split-GFP complementation and the yeast
156 split-ubiquitin assays. The co-immunoprecipitation (co-IP) results also demonstrated that
157 GFP-*At*CNIH5 interacts with the endogenous *At*PHT1;1/2/3 proteins. The *cnih5* mutant
158 exhibits reduced shoot Pi levels, decreased *At*PHT1s, and increased *At*PHF1
159 accumulation. Consistently, the PM localization of split-GFP tagged-*At*PHT1;1 is
160 diminished in the epidermis of the root transition/elongation zone and the root hair. The
161 characterization of *cnih1/5*, *cnih3/5,* and *cnih4/5* double mutants further suggested that
162 *At*CNIH5 is the primary *At*CNIH member regulating the cellular Pi homeostasis during
163 the seedling stage. Moreover, our genetic studies suggest that dysfunctional *At*CNIH5
164 alleviates the Pi toxicity of the Pi overaccumulator *pho2*, supporting a role for *At*CNIH5
165 in regulating Pi homeostasis. Nevertheless, neither *At*CNIH5 interacts with *At*PHO2 *in*
166 *planta*, nor does the transient expression of *At*PHO2 downregulate the expression of
167 *At*CNIH5, arguing against *At*CNIH5 as a direct target of the *At*PHO2 regulatory module.
168 Overall, our findings demonstrate that loss of *AtCNIH5* leads to a lower PM targeting
169 efficiency of *At*PHT1s and reveal *At*CNIH5 as a *bona fide* ER cargo receptor that
170 interplays with *At*PHF1 to ensure efficient trafficking of *At*PHT1s to the cell surface.
171

172 **Results**

173 ***At*CNIH5 is induced by Pi deficiency preferentially in the outer root cell layers**

174 Previous RNA-seq analysis (Liu *et al.*, 2016) suggested that *AtCNIH* gene members
175 exhibit comparable expression levels in the roots of young seedlings, except *AtCNIH2*,
176 whose expression was barely detectable (Fig. S1). To corroborate the responsiveness of

177 *AtCNIH5* to Pi starvation, we examined the transcript expression of *AtCNIH1, AtCNIH3,*
178 *AtCNIH4*, and *AtCNIH5* by RT-qPCR. The expression of *AtCNIH5* remarkably increased
179 in both the shoot and root following Pi starvation (**Fig. 1A**). In contrast, *AtCNIH3* and
180 *AtCNIH4* were upregulated by nitrogen (N) deprivation (**Fig. 1A**). We analysed the
181 spatial expression pattern of *AtCNIH5* using promoter: *uidA* (a gene encoding β-
182 glucuronidase or GUS) fusion lines. Under full-nutrient conditions, the promoter activity
183 of *AtCNIH5* was found in the trichomes and the vascular tissues of the shoot (**Fig. 1B**).
184 In the primary root, the expression of *AtCNIH5* was absent in the root cap and meristem
185 but strongly expressed in the stele of the transition/elongation and nearly all cell types in
186 the differentiation/maturation zones (**Fig. 1B**). In the lateral root, *AtCNIH5* was expressed
187 in the vascular tissues and detectable in the columella (**Fig. 1B**). Interestingly, the
188 promoter activity of *AtCNIH5* was markedly elevated in the epidermal, cortical, and
189 endodermal cells of the primary root following Pi deprivation (**Fig. 1B**). In comparison,
190 the promoter activities of *AtCNIH1*, *AtCNIH3*, and *AtCNIH4* were confined to the
191 vascular tissues of the primary root, regardless of nutrient conditions (Fig. S2A**)**, and also
192 observed in the columella of the lateral root (Fig. S2B). Characterization of *AtCNIH5pro*:
193 GFP fusion lines at the young seedling stage recapitulated that, irrespective of Pi regimes,
194 *AtCNIH5* is expressed in the root transition/elongation and differentiation/maturation
195 zones and root hairs (Fig. S3). Collectively, the expression of *AtCNIH5* is enhanced by
196 Pi starvation, and its promoter activity is upregulated by low Pi in the outer root cell
197 layers.
198
199 ***At*CNIH5 resides both at the ER and ERES**
200 Previous studies of the pollen-specific expression of *At*CNIHs showed their
201 distribution at the ER (Wudick *et al.*, 2018). Furthermore, RFP-*At*CNIH4 could be
202 detected at the pollen tube's PM and colocalized with the ERES marker *At*SEC24A
203 (Wudick *et al.*, 2018). To examine the subcellular distribution of *At*CNIH5 in other
204 tissues, we generated the construct encoding UBQ10 promoter-driven β-estradiol-
205 inducible *At*CNIH5 tagged with the 10th β-strand of GFP (*UBQ10*:*sXVE*: S10-*At*CNIH5)
206 for transient expression. In *N. benthamiana* leaves, the split-GFP self-complementation
207 allows live-cell imaging of S10-tagged fusion proteins in the presence of the detector
208 S11-GFP1–9 (Liu *et al.*, 2018, Liu, 2021). The distribution of S10-*At*CNIH5 showed a

209 typical ER-network pattern when co-expressed with the cytosolic S11-GFP1–9 (**Fig. 2A**),
210 indicating that the N-terminus of *At*CNIH5 is in the cytoplasm. While S10-*At*CNIH5
211 colocalized with the ER-luminal marker mCherry-HDEL, the mCherry-*At*CNIH5-labeled
212 punctate structures distributed on the ER tubules and sheet rims and were closely
213 associated with the ERES marker *At*SEC16A/MAG5 (Takagi *et al.*, 2013) (**Fig. 2A**).
214 Taking advantage of high-resolution confocal microscopy, we measured the distance
215 between the red fluorescence protein-tagged *At*CNIH5 and the *cis*-Golgi marker MNS1
216 (Liebminger *et al.*, 2009) and the three ERES markers *At*SAR1A-GFP, GFP-*At*SEC16A,
217 and GFP-*At*SEC24A. Our results demonstrated that both the constitutively expressed
218 RFP-*At*CNIH5 and the inducibly expressed mCherry-*At*CNIH5 significantly colocalized
219 with the tested ERES markers but not with the *cis*-Golgi marker MNS1-eGFP (**Fig. 2B**,
220 **2C**).
221 To validate the subcellular localization of *At*CNIH5 in stable lines, we used *cnih5* as
222 the genetic background to obtain transgenic plants carrying the genomic sequence of
223 *AtCNIH5* translationally in-frame with GFP (*AtCNIH5pro*: GFP-*AtCNIH5*). Two
224 independent lines showed a modest increase in shoot biomass and restored the shoot Pi
225 content to wild-type (WT)-like levels, while their shoot Pi concentrations were lower—
226 though not significantly—than those of the *cnih5* mutant (Fig. S4A), suggesting an
227 inverse relationship between shoot fresh weight and Pi levels in these lines. After
228 enriching microsomal fractions, we also detected the expression of GFP-*AtCNIH5*
229 proteins in Pi-limited roots using anti-*At*CNIH5 antibody (Fig. S4C). However, it is
230 technically challenging to determine whether GFP-*AtCNIH5* proteins are more abundant
231 than the endogenous *At*CNIH5 proteins in WT plants due to differences in molecular
232 weight between GFP-*AtCNIH5* and *At*CNIH5. Under the confocal microscope, the
233 signals of GFP-*AtCNIH5* in the Pi-limited roots appeared faint overall. Nonetheless, when
234 images were acquired using Airyscan mode, the punctate structures in the root hair and
235 root epidermal cells became more pronounced (**Fig. 2D**). These observations suggested
236 that the localization of *At*CNIH5 at the ER and ERES in *N. benthamiana* leaves was
237 unlikely to be an artifact of overexpression.
238
239 ***At*CNIH5 interacts with *At*PHT1s and *At*PHF1**
240 The yeast split ubiquitin-based interactome revealed the interaction of *At*CNIH1 with

241 *At*PHT1;9 and *At*PHF1 (Jones Alexander *et al.*, 2014), prompting us to test whether
242 *At*CNIH5 also interacts with *At*PHT1s and *At*PHF1. Considering the expression of
243 *AtCNIH5* and *AtPHT1;1* mainly in the root epidermis, we selected *At*PHT1;1 to represent
244 *At*PHT1s in this study. In agro-infiltrated *N. benthamiana* leaves, S10-*At*CNIH5
245 interacted with the 11th β-strand of sfGFP-tagged *At*PHT1;1 (*At*PHT1;1-S11), as
246 manifested by the reconstituted GFP signals in the presence of the cytosolic GFP1–9 (Liu
247 *et al.*, 2018, Liu, 2021) (**Fig. 3A**). *At*CNIH5 and *At*PHF1 have a similar membrane
248 topology, making the tripartite split-GFP complementation method unsuitable for
249 detecting their interaction. Therefore, we used the conventional bipartite split-GFP
250 complementation method, known as bimolecular fluorescence complementation (BiFC),
251 to investigate their interaction. However, we were unable to demonstrate an interaction
252 between these two proteins because positive controls failed. We then exploited the yeast
253 split-ubiquitin system (SUS) to examine the interaction of *At*CNIH5 with *At*PHT1;1,
254 *At*PHT1;4, and *At*PHF1. The results of the nutrient selection and the LacZ β-galactosidase
255 assays suggested that *At*CNIH5 interacted with these proteins (**Fig. 3B**). Since the amino
256 acid sequences of *At*PHT1s share over 47.4% identity, we demonstrated that *At*CNIH5
257 also interacts with *At*PHT1;2, *At*PHT1;5, *At*PHT1;7 and *At*PHT1;9 in our side-by-side
258 study (Liu *et al.*, 2024), indicating that *At*CNIH5 recognizes conserved motifs within the
259 *At*PHT1 family. Furthermore, we performed co-IP using *Arabidopsis* transgenic plants
260 harbouring the genomic GFP-*AtCNIH5* (*AtCNIH5pro*: GFP-*AtCNIH5/cnih5*) or the free
261 GFP under the UBQ10 promoter. As the cytosolic GFP was nearly 20 times more
262 abundant than GFP-*AtCNIH5* in the root low-speed pellet (LSP) membrane fraction, we
263 calculated that approximately 40 times more endogenous *At*PHT1;1/2/3 and *At*PHF1
264 proteins were co-immunoprecipitated with GFP-*AtCNIH5* than with GFP (**Fig. 3C**).
265 These results supported that *At*CNIH5 interacts with *At*PHT1s and *At*PHF1.
266

267 **Loss of *AtCNIH5* confers reduced Pi levels, *At*PHT1s accumulation, and Pi transport**

268 To determine the physiological role of *At*CNIH5, we grew WT and *cnih5* mutants
269 under different Pi regimes. Regardless of Pi status, the shoot and root fresh weight of
270 *cnih5* mutants showed no differences from that of WT (**Fig. 4A**). In contrast, the shoot Pi
271 level of *cnih5* diminished by 18% compared to WT under Pi sufficiency (**Fig. 4B**). We
272 could rescue both the lower shoot Pi concentrations and Pi content in *cnih5* under Pi

273 sufficiency by introducing the genomic construct encoding *At*CNIH5 (*AtCNIH5pro*:
274 *AtCNIH5*) (Fig. S4B), indicating that the reduced Pi accumulation in *cnih5* was attributed
275 to the non-functional *cnih5* allele. While the protein expression of the *AtCNIH5* transgene
276 in the two independent lines was similar to the endogenous *At*CNIH5 levels in WT, the
277 third line exhibited a 4.4-fold increase in *At*CNIH5 protein levels and grew slightly larger
278 than WT (Fig. S4B, S4C). These findings are consistent with the restored shoot Pi content
279 *per* plant and the inverse relationship between the shoot fresh weight and the shoot Pi
280 levels noted in the GFP-*AtCNIH5*-complemented lines (Fig. S4A). We inferred that the
281 increased shoot biomass of GFP-*AtCNIH5* complemented lines was likely due to the
282 enhanced expression or activity of GFP-*AtCNIH5* compared to that of the genomic
283 *AtCNIH5* transgene.

284 The lower shoot Pi levels in *cnih5* did not lead to the upregulation of several Pi
285 starvation-induced genes in the root, except for *AtPHT1;4* (Fig. S5A). The primary root
286 length was slightly shorter in *cnih5* than in WT regardless of Pi regimes, while the lateral
287 root density in *cnih5* was significantly higher than in WT under Pi sufficiency (Fig. S5B,
288 S5C). In addition, *cnih5* exhibited shorter root hair lengths than WT, but there was no
289 difference in root hair density between WT and *cnih5* (Fig. S5E, S5F). To evaluate
290 whether *At*PHT1s account for the decreased Pi levels in *cnih5*, we examined the
291 abundance of *At*PHT1;1/2/3 and *At*PHT1;4 proteins, which are the prominent *At*PHT1
292 members involved in Pi uptake (Shin *et al.*, 2004, Ayadi *et al.*, 2015). Given that the
293 impaired ER exit of *At*PHT1s in *phf1* caused a reduction in *At*PHT1;1/2/3 and *At*PHT1;4
294 proteins (Huang *et al.*, 2013), we hypothesized that PM proteins retained inside the cell
295 are eventually targeted for degradation due to protein quality control. Based on this,
296 defective *At*CNIH5 would reduce the steady-state levels of *At*PHT1;1/2/3 and *At*PHT1;4.
297 Although the expression of *AtCNIH1*, *AtCNIH3*, and *AtCNIH4* was of a similar
298 magnitude in our qRT-PCR results (**Fig. 1A**), previous RNA-seq analysis (Liu *et al.*,
299 2016) suggested *AtCNIH4* as the most abundant *AtCNIH* gene member (Fig. S1).
300 Therefore, we included *cnih4* mutants for comparison. Under Pi sufficiency, the amount
301 of *At*PHT1;1/2/3 and *At*PHT1;4 in the total root proteins was indistinguishable among
302 WT, *cnih4*, and *cnih5*; however, under Pi deficiency, these proteins were decreased in
303 *cnih5* by 20–25% as compared to WT (Fig. S6). After enrichment of root membrane
304 proteins, a 50% decrease of *At*PHT1;1/2/3 was detected in *cnih5* under both Pi regimes

305 (**Fig. 4C**). The protein abundance of *At*PHT1;4 was also reduced by 40% in the root
306 membrane proteins of *cnih5* as compared with the corresponding WT controls (**Fig. 4C**).
307 Importantly, the protein abundance of *At*PHT1;1/2/3 in the Pi-limited *cnih5*
308 complemented lines either carrying *AtCNIH5pro*: GFP-*AtCNIH5* or *AtCNIH5pro*:
309 *AtCNIH5* were higher than in *cnih5* and were restored to levels comparable to or
310 exceeding those of the WT (Fig. S4C), reinforcing that *At*PHT1;1/2/3 are indeed
311 downstream effectors of *At*CNIH5.

312 We determined the Pi uptake of radioactive tracer (^{32}P) *per* plant using a real-time
313 imaging system (Kanno *et al.*, 2016). When Pi is replete, there were no significant
314 differences in the Pi uptake within 15 minutes between WT and *cnih5*; however, the
315 shoot-to-root distribution of ^{32}P significantly decreased in *cnih5* (**Fig. 4D**). This may be
316 attributed to an additional role of *At*CNIH5 in the translocation of Pi from roots to shoots
317 under Pi sufficiency by facilitating the PM targeting of *At*PHT1 transporters in different
318 root cell types, as several *AtPHT1* genes are expressed in the vascular tissues (Nussaume
319 *et al.*, 2011). Under Pi deficiency, loss of *AtCNIH5* resulted in an 18% reduction of ^{32}P
320 uptake relative to the WT, while the shoot-to-root distribution of ^{32}P was comparable
321 between the two genotypes (**Fig. 4D**), suggesting that *At*CNIH5 is more critical for Pi
322 uptake under Pi limitation. Overall, *cnih5* exhibited lower shoot Pi accumulation under
323 Pi sufficiency due to the reduced translocation of Pi from roots to shoots and showed
324 decreased Pi uptake under Pi deficiency, which could be ascribed to the decreased protein
325 amount of *At*PHT1;1/2/3 and *At*PHT1;4, and probably other *At*PHT1s as well.

326 To answer whether *At*CNIH5 shares functional redundancy with other *At*CNIH
327 members, we analysed *cnih* double mutants carrying defective *AtCNIH1*, *AtCNIH3*, or
328 *AtCNIH4* in the *cnih5* background. In the respective *cnih* double mutants, the expression
329 of the remaining *AtCNIH* genes was not altered (Fig. S7A), hinting that there is no
330 compensatory upregulation of other *AtCNIH* genes at the transcript level when *AtCNIH5*
331 and/or other *AtCNIH* are knocked out. Compared to *cnih5*, all the *cnih* double mutants
332 did not display a greater reduction in fresh weight and Pi levels (Fig. S7B, S7C). Taken
333 together, *At*CNIH5 is the predominant *At*CNIH member functionally linked to the
334 regulation of Pi transport.

335

336 **Loss of *AtCNIH5* leads to decreased plasma membrane localization of *At*PHT1;1**

337 To prove that *At*CNIH5 is a *bona fide* ER cargo receptor of *At*PHT1s, we sought to
338 check the subcellular distribution of *At*PHT1;1 in *cnih5*. For equal transgene expression,
339 a homozygous line (*At*PHT1;1-S11/GFP1–10) co-expressing *At*PHT1;1-S11 driven by
340 the native *At*PHT1;1 promoter and GFP1–10 driven by the 35S promoter was generated
341 in the WT background and outcrossed to the *cnih5* mutant. The F2 progeny were screened
342 for moderate fluorescence signals and subjected to genotyping. F3 individuals propagated
343 from the F2 plants with either the WT (+/+) or *cnih5* (–/–) background were used for
344 confocal imaging analysis. Under Pi sufficiency, the fluorescence signals of *At*PHT1;1-
345 S11/GFP1–10 plants in the WT background were relatively weak. Therefore, we focused
346 on the subcellular localization of *At*PHT1;1-S11 in the area where *AtPHT1;1* is expressed
347 under Pi limitation. In the WT background, *At*PHT1;1-S11 accumulated at the PM in the
348 root epidermis of the transition/elongation zone (**Fig. 5A**, **5B**) and the root hairs of the
349 differentiation/maturation zone (**Fig. 5C**). By contrast, *At*PHT1;1-S11 in the *cnih5*
350 background occasionally distributed into the intracellular reticular or punctate structures
351 in these regions (**Fig. 5B**, **5C**, and **Table 1**), and the fluorescence signals significantly
352 declined at the PM by nearly 50% (**Fig. 5A**, **5C**). Hence, we conclude that *At*CNIH5
353 facilitates the ER export and thus the PM targeting of *At*PHT1;1, particularly in the
354 elongating root epidermis and root hair.
355
356 ***At*CNIH5 and *At*PHF1 act in concert to control the ER exit of *At*PHT1s**
357 The ER-resident *At*PHF1 was previously known to regulate the ER exit of *At*PHT1s.
358 We thus conjectured whether the decreased PM targeting of *At*PHT1s in *cnih5* is
359 indirectly due to an altered protein abundance of *At*PHF1. To our surprise, *At*PHF1
360 increased by nearly 1.3-fold in the root total proteins of *cnih5* under both Pi regimes (Fig.
361 S6), even though the transcript level of *AtPHF1* was not upregulated (Fig. S5A). These
362 results implied that *At*PHF1 is likely upregulated to compensate for the loss of *At*CNIH5.
363 Considering that *At*CNIH5, as well as *At*PHF1, interacts with *At*PHT1;1, we suspected
364 that *At*CNIH5 collaborates with *At*PHF1 to assist the ER exit of *At*PHT1s. To explore this
365 possibility, we characterized *phf1/cnih4*, *phf1/cnih5*, and *phf1/cnih4/5* mutants.
366 Compared to the *phf1* seedlings, the shoot and root biomass of *phf1/cnih5* and
367 *phf1/cnih4/5* mutants were further reduced (**Fig. 6A**). However, *phf1/cnih5* mutants
368 showed no differences in the shoot and root Pi levels compared to the *phf1* (**Fig. 6B**),

369 suggesting that *phf1* is epistatic to *cnih5*. In accordance with these results, the protein
370 amount of *At*PHT1;1/2/3 in the total root proteins was comparable in these mutants (**Fig.**
371 **6C**). During the adult-plant stage in hydroponic solutions, the *phf1/cnih4*, *phf1/cnih5*, and
372 *phf1/cnih4/5* mutants also displayed reduced shoot growth relative to the *phf1* (Fig. S8A).
373 Of note, the *phf1/cnih5* and *phf1/cnih4/5* plants exhibited reduced shoot Pi levels relative
374 to the *phf1* under Pi sufficiency (Fig. S8B). Therefore, the extra loss of *AtCNIH5* in the
375 *phf1* background aggravates the growth retardation and further reduces shoot Pi
376 accumulation when plants grow to an older stage, indicating a complex genetic interaction
377 between *At*PHF1 and *At*CNIH5.
378
379 ***At*CNIH5 alleviates the Pi toxicity of *pho2* but is unlikely to be a direct target of**
380 ***At*PHO2**
381 To address whether *At*CNIH5 acts downstream of the *At*PHO2-mediated Pi
382 homeostasis pathway, we generated the *pho2/cnih5* mutant. Compared to *pho2*,
383 *pho2/cnih5* accumulated less Pi in the shoot to a similar extent as reported for *pho2/pht1;1*
384 (**Fig. 7A**) (Huang *et al.*, 2013) and exhibited reduced levels of *At*PHT1;1/2/3 and
385 *At*PHT1;4 relative to the *pho2* (**Fig. 7B**). By comparison, the protein level of the xylem
386 loading Pi transporter *At*PHO1 was increased in *pho2/cnih5* (**Fig. 7B**). The upregulation
387 of *At*PHO1 was also observed in the *cnih5* mutant regardless of Pi regimes (Liu *et al.*,
388 2024), suggesting that defective *AtCNIH5* specifically impairs the ER export of *At*PHT1s.
389 We next explored whether *At*PHO2 functions as a hypothesized E2/E3 hybrid enzyme to
390 mediate the downregulation of *At*CNIH5. It has been shown that the C748A mutation of
391 *At*PHO2 disrupts the conserved catalytic cysteine residue necessary for *At*PHO2-
392 mediated degradation of *At*PHO1 (Liu *et al.*, 2012). Therefore, we utilized this variant in
393 the protein-protein interaction assay to avoid substrate or protein degradation. Using the
394 *N. benthamiana* transient expression system, we found that, in contrast to *At*PHO2-
395 mediated degradation of *At*PHO1 in a dosage-dependent manner as previously reported
396 (Liu et al., 2012), neither the catalytically defective *At*PHO2^{C748A} interacted with
397 *At*CNIH5 nor the catalytically active *At*PHO2 suppressed the expression of *At*CNIH5
398 (Fig. S9A, S9B). Taken together, the loss of *AtCNIH5* alleviates the Pi toxicity of *pho2*
399 due to downregulation of *At*PHT1s, but we have no evidence to support *At*CNIH5 as a
400 direct target of *At*PHO2.

401

402 **Discussion**

403 ***At*CNIH5 is a Pi starvation-induced and cell type-specific ER cargo receptor for**
404 ***At*PHT1s**

405 Our study provides multiple lines of evidence showing that *At*CNIH5 is a Pi starvation-
406 induced ER cargo receptor that facilitates the PM targeting of *At*PHT1s. Gene expression
407 profiles using GUS and GFP reporters and subcellular distribution analyses of fluorescent
408 protein fusions suggest *At*CNIH5 as the sole *At*CNIH member induced by low Pi in the
409 root outer layers (**Fig. 1A**, **1B**, and Fig. S2A, S2B, and S3). We also showed that
410 *At*CNIH5 localized to the ER and was closely associated with the ERES markers
411 *At*SAR1A, *At*SEC16A, and *At*SEC24A (**Fig. 2A–C**). As *At*CNIH5 interacts with nearly
412 all the *At*PHT1 family members (**Fig. 3A–C**) (Liu *et al.*, 2024), *At*CNIH5 likely
413 participates in the COPII-mediated ER-to-Golgi transport of all *At*PHT1s. We surmise
414 that the recognition of *At*PHT1s by *At*SEC24s alone is not an efficient signal to drive the
415 ER exit of *At*PHT1s, and therefore requires the coincident or successive interaction of
416 *At*PHT1s with *At*CNIH5 and *At*PHF1 (see the discussion in the next section). Although
417 *AtCNIH5* is expressed at a slightly lower level than *AtCNIH1*, *AtCNIH3,* and *AtCNIH4*
418 under Pi sufficiency (Liu *et al.*, 2016), the impairment of *AtCNIH5* diminished the amount
419 of *At*PHT1;1–1;4 by 40–50% in the root microsomal fractions (**Fig**. **4C**). The results of
420 confocal imaging also corroborated a lower efficiency of PM targeting and higher
421 intracellular retention of *At*PHT1;1-S11 in the epidermis within the root
422 transition/elongation zone and the root hair of *cnih5* (**Fig. 5A–C**, **Table 1**). Our recent
423 side-by-side membrane proteomic analysis identified *At*PHT1s as the prominent
424 membrane cargoes of *At*CNIH5 under Pi starvation (Liu *et al.*, 2024), reinforcing the
425 conclusion that *At*CNIH5 mediates the ER export of *At*PHT1s and, thus, their PM
426 targeting. Since the promoter activities of *AtCNIH1*, *AtCNIH3,* and *AtCNIH4* are barely
427 detected in the epidermal, and cortical, and endodermal cells of the primary root (Fig.
428 S2A), where *AtPHT1;1–1;4* genes are mainly expressed, we infer that *At*CNIH5 is the
429 predominant *At*CNIH member regulating the PM trafficking of *At*PHT1;1–1;4 in these
430 cell layers. However, we cannot exclude the possibility that, in addition to *At*CNIH5,
431 other *At*CNIH members or pairs of *At*CNIHs also mediate the ER export of *At*PHT1
432 transporters in vascular tissues, even though we did not observe any exacerbated

433 phenotypes of *cnih1/5*, *cnih3/5,* and *cnih4/5* double mutants. Our yeast SUS showed that
434 *At*PHT1;1 also interacts with *At*CNIH1, *At*CNIH3*,* and *At*CNIH4 (Fig. S10A), implying
435 that different *At*CNIH members could recognize *At*PHT1;1 as their membrane cargo, at
436 least in the yeast heterologous expression system. Of note, we observed a strikingly
437 reduced shoot-to-root distribution of newly taken up Pi in *cnih5* under Pi sufficiency (**Fig.**
438 **4D**), indicating that *At*CNIH5 also participates in regulating Pi translocation within plants.
439 This finding aligns with the previously reported but often overlooked role of *At*PHT1;1
440 in the root-to-shoot translocation of Pi when Pi is abundant (Ayadi *et al.*, 2015).
441 While the *AtCNIH4* transcript is the most abundant in its family according to RNA-
442 seq data (Liu *et al.*, 2016) (Fig. S1), the phenotypes of *cnih4* and *cnih4/5* indicate that
443 *At*CNIH4 plays a minor role in modulating Pi homeostasis during the seedling stage.
444 *At*CNIH isoforms have the potential to form tissue- or cell-type-dependent oligomers
445 (Wudick *et al.*, 2018), which may affect the ER export of *At*PHT1s to varying degrees.
446 Intriguingly, belonging to the *Brassicaceae* family, which is devoid of mycorrhizal
447 symbiosis, the *Arabidopsis* species was suggested to utilize rapid root growth and root
448 hair formation as a strategy for Pi uptake when grown under Pi depletion (Lambers *et al.*,
449 2008). In agreement with this notion, we observed a less apparent reduction of Pi level in
450 the 11-day-old *cnih5* seedlings (reduction by 18%; **Fig. 4B**) than in the 5-day-old *cnih5*
451 seedlings (reduction by 30%; Fig. S5D), in which macro-scale architectures of the root
452 system were still undeveloped. Based on the PANTHER classification
453 (http://www.pantherdb.org/), *Arabidopsis thaliana* CNIH1 (*At*CNIH1) and *Os*CNIH2 are
454 grouped into the same subfamily as the *yeast* Erv14 and its paralog Erv15; *At*CNIH2,
455 *At*CNIH4, and *Os*CNIH1 belong to the same subfamily; *At*CNIH3 and *At*CNIH5 are
456 *Brassicaceae*-specific CNIH paralogs (Fig. S11). In other words, our data support the
457 notion that the *Brassicaceae*-specific *At*CNIH5 may have a unique physiological function
458 and plays a more crucial role in enhancing Pi transport in the elongating root epidermis
459 and root hairs at the early seedling stage. A previous study on functional complementation
460 in yeast showed that *Sc*Erv14, *At*CNIH1, *At*CNIH3, and *At*CNIH4, but not *At*CNIH2 and
461 *At*CNIH5, enhanced the tolerance of the Δ*erv14* mutant to NaCl to various degrees
462 (Wudick *et al*., 2018), suggesting cargo specificity among *At*CNIHs. In our recent study,
463 we identified additional potential membrane cargoes of *At*CNIH5 beyond *At*PHT1s (Liu
464 *et al*., 2024). Interestingly, the first transmembrane domain of *At*CNIH5 is sufficient to

465 interact with *At*PHT1;1, whereas the C-terminal acidic residue of *At*CNIH5 is required
466 for interacting with *At*OCT1 but not with *At*PHT1;1 or *At*DTX21 (Liu *et al*., 2024).
467 Therefore, it is likely that *At*CNIH5 interacts with *At*PHT1s using a mechanism distinct
468 from those used by the acidic domain of fungal and rice CNIHs for their cognate cargoes.
469

470 **The interplay of *At*PHF1 and *At*CNIHs in regulating the ER exit of *At*PHT1s**

471 *AtPHF1* is mainly expressed in the root tip and stele under Pi sufficiency and can be
472 further induced in the external root layers at low Pi availability (Bayle *et al.*, 2011). This
473 pattern coincides with the Pi starvation-induced expression of *AtCNIH5* in the epidermis
474 and cortex, whereas the gene activity of *AtCNIH5* is absent in the root apical meristem
475 (**Fig. 1B**, Fig. S3). Although the compensation mechanism underlying the upregulation
476 of *At*PHF1 in *cnih5* remains obscure (Fig. S6), the additional loss of *AtCNIH5* in the *phf1*
477 did not synergistically reduce cellular Pi levels but severed plant growth (**Fig. 6B**). This
478 led to the idea that *At*PHF1 and *At*CNIH5 may not play a functionally redundant role but
479 *At*PHF1 is epistatic to *At*CNIH5 in regulating the ER exit of *At*PHT1s. The SEC12-related
480 plant-specific PHF1 was previously proposed to functionally resemble the yeast ER-
481 resident protein Pho86 (González *et al.*, 2005). As the *in vitro* vesicle budding assay
482 indicated, the yeast Pho86 may assume a conformation of Pi transporter Pho84 competent
483 for specific incorporation into COPII vesicles or to recruit COPII proteins to the ER (Lau
484 *et al.*, 2000). By comparison, the yeast Erv14 cycles between the ER and the Golgi, and
485 the ER membranes lacking functional Erv14 exhibit less efficient incorporation of
486 cargoes into COPII vesicles (Powers & Barlowe, 2002). In accordance, the live-cell
487 imaging results revealed a reduction in the kinetics of ER exit of Erv14's cargoes in the
488 *erv14Δ* mutant (Herzig *et al.*, 2012). Their findings align with our current view on the
489 role of *At*CNIH5 in promoting the ER export of *At*PHT1s. While split-GFP-tagged
490 *At*PHT1;1 was mainly distributed at the PM of root cells in the WT under Pi depletion, it
491 was in part retained intracellularly in the epidermis within the root transition/elongation
492 zone and the root hair of *cnih5* (**Fig. 5B**–**C**, **Table 1**, and Fig. S12). These observations
493 suggested that PM targeting of *At*PHT1;1 is less efficient in the absence of *At*CNIH5. By
494 contrast, *At*PHT1;1-S11 in the *phf1* was barely detectable at the PM of the epidermal cells
495 throughout the different developmental zones, including the lateral root cap (Fig. S12).
496 Unlike the unicellular yeast, we envisage that higher plants have adopted a mechanism to

497 jointly engage PHF1 and CNIHs in specific cell types, thereby selecting and packaging
498 PHT1s for efficient COPII-mediated transport. Indeed, our recent study unveiled that
499 *At*PHF1 interacts with *At*SAR1 GTPase, a key protein that initiates the assembly of
500 COPII, and thus likely participates in the early step of COPII recruitment for the ER
501 export of PHT1s (Lung *et al.*, 2025). By contrast, *At*CNIH5 impacts the efficiency of PM
502 trafficking of *At*PHT1s, particularly in the elongating root epidermis and root hairs (**Fig.**
503 **5A−C**). As the proliferation of root hair is a crucial trait for improving Pi acquisition
504 under Pi limitation (Gahoonia & Nielsen, 1998, Tanaka *et al.*, 2014), it would be
505 interesting to investigate the physiological relevance of *At*CNIH5 in modulating the PM
506 trafficking of *At*PHT1s in root hair cells. It is also worth mentioning that in the yeast SUS,
507 *At*PHF1 interacts with *At*CNIH1, *At*CNIH3, and *At*CNIH4 much less strongly than with
508 *At*CNIH5 (Fig. S10B). This implied that even in the vascular tissues, where *AtPHF1* and
509 *AtCNIH* genes are highly expressed, *At*PHF1 may preferentially interact with *At*CNIH5
510 over the other *At*CNIH isoforms. According to single-cell mRNA sequencing (scRNA-
511 seq) analyses under high Pi conditions, *AtCNIH1* is mainly expressed in the proliferation
512 and transition domains, with a higher expression level in the phloem of the proliferation
513 domain. *AtCNIH3* is also primarily expressed in the proliferation and transition domains,
514 yet at a lower level, and its expression gradually decreases along the developmental axis
515 as cells differentiate. *AtCNIH4* is expressed in all cell types of the proliferation and
516 transition domains, and strongly expressed in the epidermis of the elongation and
517 maturation domains. *AtCNIH4* and *AtCNIH5* are the most abundant members in
518 epidermal cells among the family. In addition, *AtCNIH5* shows a trend of gradually
519 increased expression in the root epidermis and cortex along the developmental axis and
520 high expression in the stele of the maturation zone (Fig. S13) (Shahan *et al.*, 2022, Trevor
521 *et al.*, 2022). This highlights a significant role for *At*CNIH5 in facilitating Pi uptake and
522 Pi translocation beyond the root apical meristem, primarily in the outer layers of the non-
523 proliferating root cells upon Pi starvation. Nonetheless, we cannot exclude the possibility
524 that the lack of *At*PHF1 and *At*CNIH5 further suppressed the plant growth due to
525 exaggerated cytoplasmic Pi inadequacy. Alternatively, but not mutually exclusive to this
526 scenario, *At*CNIH5 may have some downstream effectors other than *At*PHT1s that
527 exacerbate the growth retardation of *phf1/cnih5* (Liu *et al.*, 2024). On the basis of our
528 present study, we propose a working model as to how *At*PHF1 and *At*CNIH5 interplay to

529 assist the ER exit of *At*PHT1s (**Fig. 8**). *At*PHF1 interacts with *At*PHT1s at the ER to ensure
530 their competence for the ER exit, and likely with *At*SAR1 GTPase as well, accompanied
531 by the COPII assembly at the ERES of nearly every cell type in the root. On the other
532 hand, *At*CNIH5 acts at a later step, perhaps by selectively loading *At*PHT1s at ERES into
533 the COPII-mediated trafficking pathway in the non-dividing root cells, including the
534 epidermis within the transition/elongation zone and the elongating root hair of the
535 differentiation zone. More studies are needed to define the spatiotemporal interaction of
536 *At*PHT1s, *At*PHF1, and *At*CNIH5.
537
538 **Materials and Methods**
539 **Plant material and growth conditions**
540 All *A. thaliana* plants used in this study were in the Columbia-0 (Col-0) ecotype. Seeds
541 of wild-type (WT), *cnih4* (SALK_145991), *cnih5* (SAIL_256_B03), *phf1*
542 (SALK_037068), and *pho2-1* (Delhaize & Randall, 1995) were obtained from the
543 Arabidopsis Biological Resource Center (ABRC). The *cnih1/5* (SAIL_117_E12 for *cnih1*
544 and SAIL_256_B03 for *cnih5*) and *cnih3/5* (GABI_300F09 for *cnih3* and
545 SAIL_256_B03 for *cnih5*) mutants were genotyped as previously described (Wudick *et*
546 *al.*, 2018). *A. thaliana* seeds were surface-sterilized, germinated, and grown on plates
547 with modified one-half strength (1/2) Hoagland nutrient solution containing 250 μM
548 KH_2PO_4, 1% sucrose, and 0.8 or 1.2% Bacto agar (BD Difco™ 214010) in the growth
549 chamber at 22°C with a 16-h light/8-h dark cycle. The Pi-sufficient (+P, 250 μM KH_2PO_4)
550 and Pi-deficient (−P, 0 μM KH_2PO_4) media were modified 1/2 Hoagland nutrient. The
551 N-deficient (−N, 0 μM and 0.1 mM KNO_3) media were modified 1/2 Hoagland nutrient
552 solutions. For hydroponic growth of *A. thaliana* adult plants, 1–2-week-old seedlings
553 were transferred to +P (250 μM KH_2PO_4) modified 1/2 Hoagland solutions without a
554 supplement of sucrose and grown for additional days in +P (250 μM KH_2PO_4) or −P (10
555 μM KH_2PO_4) media as indicated in figure legends. For *Nicotiana benthamiana* (*N.*
556 *benthamiana*) plants, seeds were surface-sterilized and germinated on 1/2 Murashige and
557 Skoog (MS) medium. Three- to four-week-old plants were used for infiltration of
558 *Agrobacterium tumefaciens* (*A. tumefaciens*).
559
560 **Genomic DNA extraction and genotyping of mutants**

561 Genomic DNA was extracted from the leaves of 2-week-old plants with the extraction
562 buffer containing 200 mM Tris-HCl (pH 7.5), 250 mM NaCl, 25 mM EDTA (pH 8.0),
563 and 0.5% SDS. Polymerase chain reaction (PCR) was then performed to validate the
564 presence of the T-DNA alleles of *phf1*, *cnih4*, *cnih5*, and the *pho2* point mutation in
565 samples as previously described. Primer sequences used are listed in Table S1.
566
567 **RNA isolation, reverse transcription PCR (RT-PCR), and quantitative RT-PCR**
568 Total root RNA was isolated using GENEzol™ TriRNA Pure Kit with DNase
569 (Geneaid), and a 500-ng RNA was used for the first-strand cDNA synthesis using
570 PrimeScript™ 1st strand cDNA Synthesis Kit (TaKaRa) with oligo(dT) primer.
571 Quantitative RT-PCR (RT-qPCR) was performed using KAPA SYBR® FAST qPCR
572 Master Mix (2×) Kit (Kapa Biosystems) on StepOnePlus™ Real-Time PCR System
573 (Applied Biosystems) according to the manufacturer's instructions. Gene expression
574 values were normalized to the internal reference *ACT8* (AT1G49240). Transcript
575 expression levels of *AtCNIH* genes in WT, *cnih* single, and *cnih* double mutants were
576 examined by RT-PCR or RT-qPCR. Primer sequences used are listed in Table S1.
577
578 **Construct design and yeast split-ubiquitin assay**
579 For constructing the yeast expression clones, the coding sequence (CDS) of *AtCNIH1,*
580 *AtCNIH3, AtCNIH4, AtCNIH5* and *AtPHT1;4* was amplified by PCR, cloned into the
581 pCR8/GW/TOPO vectors, and sequenced. The pCR8/GW/TOPO constructs containing
582 the CDS of *AtPHT1;1* and *AtPHF1* were cloned as previously reported (Huang *et al.*,
583 2013). The CDS of *AtCNIH5* was recombined into the synthesized MET17-PLV-
584 Cub_GW through an LR reaction, resulting in the N-terminally fused PLVCub-*At*CNIH5.
585 The CDS of *AtPHT1;1* and *At*PHF1 was recombined into MetYC_GW (ABRC plasmid
586 CD3-1740; Obrdlik *et al.*, 2004), resulting in the C-terminally fused CubPLV fragments.
587 The CDS of *AtCNIH1, AtCNIH3, AtCNIH4, AtCNIH5*, *AtPHF1*, *AtPHT1;1*, and
588 *AtPHT1;4* was recombined into NX32_GW (ABRC plasmid CD3-1737) through LR
589 reactions, resulting in the N-terminally fused Nub fragments (Obrdlik et al., 2004). The
590 Nub and Cub expression clones were sequentially transformed into the yeast THY.AP4
591 strain (ABRC CD3-808; Obrdlik et al., 2004). Fresh yeast colonies picked from Yeast
592 Extract Peptone Dextrose Adenine (YPDA) medium or Synthetic Complete (SC) medium

593 without leucine (SC–L) were inoculated in the corresponding liquid medium and
594 incubated overnight at 30°C with shaking at 200 rpm. Overnight yeast culture was then
595 diluted to OD_{600} = 0.2 and grown for another 5–12 h until OD_{600} reached 0.8. Yeast pellet
596 was collected by centrifugation at 2,000×g at 4°C for 5 min, washed with ddH_2O, and
597 resuspended in Tris-EDTA/lithium acetate solution (TE/LiAc, 10 mM Tris-HCl [pH 8.0],
598 1 mM EDTA, and 0.1 M lithium acetate). The PLVCub-*At*CNIH5, *At*PHT1;1- or
599 *At*PHF1-CubPLV-containing transformants were selected and maintained on SC–L for
600 sequential transformation with NubI (positive control), NubG (negative control), NubG-
601 *At*PHT1;1, NubG-*At*PHT1;4, NubG-*At*PHF1, NubG-*At*CNIH1, NubG-*At*CNIH3, NubG-
602 *At*CNIH4, or NubG-*At*CNIH5. Yeast transformants with Nub- and PLVCub-fusions were
603 selected and maintained on SC medium without leucine and tryptophan (SC–LW). For
604 the protein-protein interaction testing, yeast cells co-expressing Nub- and PLVCub-
605 fusions were plated on synthetic media lacking leucine, tryptophan, adenine, and histidine
606 (SC–LWAH) with 0.5 μM or 500 μM methionine or on SC–LW containing 2 g/L 5-
607 bromo-4-chloro-3-indolyl-β-d-galactopyranoside (X-Gal). Primer sequences used are
608 listed in Table S2.
609
610 **Construct design for subcellular localization analysis in *N. benthamiana* leaves**
611 For constructing the *UBQ10*:*sXVE*: S10-*At*CNIH5 and *UBQ10*:*sXVE*: mCherry-
612 *At*CNIH5 clones, the CDS of *AtCNIH5* was amplified by PCR and subcloned into
613 *UBQ10*:*sXVE*: S10-(MCS) (Addgene plasmid #108177; Liu et al., 2018, Liu, 2021). For
614 constructing the *UBQ10*: *At*SEC16A-S11 clones, the CDS of *AtSEC16A* was amplified
615 by PCR and subcloned into *UBQ10:* (MCS)-S11. The plasmid encoding *35S*: RFP-
616 *At*CNIH5 was obtained as previously reported (Wudick *et al.*, 2018). The plasmid
617 encoding *35S*: ER-mCherry (CD3-959; Nelson *et al.*, 2007) was obtained from ABRC.
618 Primer sequences used are listed in Table S2.
619
620 **Construct design for the tripartite split-GFP complementation assay in *N.***
621 ***benthamiana* leaves**
622 For constructing the *UBQ10*:*sXVE*: S10-*At*PHF1 and *UBQ10*:*sXVE*: S10-*At*PHO1
623 clones, the CDS of *AtPHF1* and *AtPHO1* were amplified by PCR and subcloned into
624 *UBQ10*:*sXVE*: S10-(MCS) (Addgene plasmid #108177; Liu et al., 2018, Liu, 2021). For

625 constructing the *UBQ10*:*sXVE*: *At*PHT1;1-S11 and *UBQ10*:*sXVE*: *At*PHO2^{C748A}-S11
626 clones, the CDS of *AtPHT1;1* and *AtPHO2* ^{C748A} were amplified by PCR and subcloned
627 into *UBQ10*:*sXVE*: (MCS)-S11 (Addgene plasmid #108179; (Liu et al., 2018, Liu, 2021).
628 For the tripartite split-GFP complementation, the constructs encoding S10-tagged and
629 S11-tagged protein fusions were co-expressed in the presence of *UBQ10*:*sXVE*: GFP1–9
630 (Addgene plasmid #108187; Liu et al., 2018, Liu, 2021). Co-expression with S10-3xHA
631 or 3xHA-S11 was a negative control for protein–protein interaction. Primer sequences
632 used are listed in Table S2.
633
634 **Construct design and protein degradation assay in *N. benthamiana* leaves**
635 For constructing *UBQ10*:*sXVE*: S10-*At*PHO2 clone, the CDS of *AtPHO2* was
636 amplified and subcloned into pGPTVII. *A. tumefaciens* carrying *UBQ10*:*sXVE*: S10-
637 *At*PHO2, *UBQ10*:*sXVE*: S10-*At*CNIH5 and *UBQ10*:*sXVE*: S10-*At*PHO1 were infiltrated
638 into *N. benthamiana* leaves, each with a final OD_{600} in the range of 0.01–0.05. *A.*
639 *tumefaciens* carrying *UBQ10*:*sXVE*: GFP (Schlücking *et al.*, 2013) was co-infiltrated as
640 an internal control at a final OD_{600} of 0.01. Primer sequences used are listed in Table S2.
641
642 ***A. tumefaciens*-mediated infiltration of *N. benthamiana* leaves**
643 *A. tumefaciens* strain EHA105 harboring the expression constructs or p19 was
644 incubated in Luria–Bertani (LB) medium with the appropriate antibiotics [gentamicin (50
645 μg ml^{-1}), rifampicin (5 μg ml^{-1}), or kanamycin (50 μg ml^{-1})]. Cells were resuspended in
646 the infiltration medium containing 10 mM $MgCl_2$, 10 mM MES (pH 7.5), and 150 μM
647 acetosyringone, and co-infiltrated into the true leaves of 3–4-week-old *N. benthamiana*
648 plants. 36.7 μM β-estradiol was applied for the inducible gene expression as previously
649 described (Liu *et al.*, 2018, Liu, 2021). The infiltrated leaves were collected 2 days post-
650 infiltration (dpi) for confocal imaging or protein extraction.
651
652 **Construct design and the generation of *A. thaliana* transgenic plants**
653 The CDS of a gene was amplified by PCR, cloned into the pJET1.2/blunt cloning
654 vector, and sequenced before subcloning into the desired expression vectors. For
655 constructing the *AtCNIH1/3/4/5pro:* GUS and *AtCNIH5pro:* GFP reporter clones (Fig.
656 S14), the genomic sequence containing the promoter region of *AtCNIH1* (−497 to +134;

657 transcription start site designated as +1), *AtCNIH3* (−1,793 to +225), *AtCNIH4* (−1,717
658 to +303), and *AtCNIH5* (−1,701 to +304) was each amplified by PCR and subcloned into
659 pMDC163 or pMDC111.
660 For constructing the *AtCNIH5* genomic clone (*AtCNIH5pro*: *AtCNIH5*) to
661 complement *cnih5*, the genomic sequence *AtCNIH5*, including the putative promoter
662 region with 5′ UTR (−1,963 to +304) and the genomic sequence containing 3′ UTR (+305
663 to +1,324), was amplified and cloned into pMDC32 using In-Fusion HD cloning
664 (TaKaRa) for sequencing. Based on the *AtCNIH5* genomic construct clone, the genomic
665 GFP-*AtCNIH5* construct (*AtCNIH5pro*: GFP-*AtCNIH5*) was generated by inserting GFP
666 at the N-terminus of *AtCNIH5* using In-Fusion HD cloning to complement *cnih5*.
667 For the subcellular localization analysis of *At*PHT1;1-S11, a homozygous line
668 expressing *35S*: GFP1–10 was established and then transformed with the *AtPHT1;1pro*:
669 *At*PHT1;1-S11 construct. For constructing the *35S*: GFP1–10 clone, the CDS of GFP1–
670 10 was amplified and subcloned into pMDC201. For constructing the *AtPHT1;1pro*:
671 *At*PHT1;1-S11 clone, the putative *AtPHT1;1* promoter sequence (−1,964 to +494) and
672 the CDS of *AtPHT1;1* were subcloned into the pGPTVII binary vector. Primer sequences
673 used are listed in Table S2.
674
675 ***A. tumefaciens*-mediated *Arabidopsis* transformation**
676 Binary expression vectors were transformed into *A. tumefaciens* strain GV3101
677 (pMP90) and then transformed into *A. thaliana* plants by the floral dip method (Clough
678 & Bent, 1998). T2 transgenic lines with a segregation ratio of 3 resistant: 1 sensitive were
679 selected for T3 propagation. Only T3 homozygous lines were used for further analyses.
680
681 **Confocal microscopy**
682 Confocal microscopy images were acquired using Zeiss LSM 800 (Zeiss) with
683 objectives Plan-Apochromat 10×/0.45 M27, 20×/0.8 M27, and 40×/1.3 Oil DIC M27 in
684 multi-track mode with line switching and an averaging of two readings. Additionally, the
685 AiryScan mode was used to enhance the acquisition of punctate structures of GFP-
686 *AtCNIH5* in *AtCNIH5pro*: GFP-*AtCNIH5/cnih5* plants. Excitation/emission wavelengths
687 were 488 nm/410−546 nm for GFP, 561 nm/560−617 nm for RFP and mCherry, and 488
688 nm/571−700 nm for FM4-64. For subcellular localization analysis of *At*PHT1;1-S11, the

689 seedlings were kept in the dark for 4 h before imaging. All the fluorescence images are
690 acquired from a single confocal optical slice.
691
692 **Line profile co-localization analysis**
693 For high-resolution co-localization of *35S:* RFP-*At*CNIH5 or *UBQ10*:*sXVE*:
694 mCherry-*At*CNIH5 with the *cis*-Golgi marker MNS1 and the three ERES markers
695 *At*SAR1A, *At*SEC16A, and *At*SEC24A in *N. benthamiana* leaves, images were acquired
696 using the line profile utility in Zeiss ZEN Blue software as previously reported
697 (McGinness *et al.*, 2025). Only well-oriented side-profile views that allowed accurate
698 visualization of cisternal separation were used for quantitative co-localization analysis.
699 For each suitable Golgi body, a line was drawn perpendicular to the organelle's long axis
700 to generate fluorescence intensity profiles for the two channels. The distance between the
701 maximum intensity peaks of each channel was measured across the line profile, providing
702 a quantitative estimate of spatial separation between fluorescent signals. Data extraction
703 and processing were automated using a Python (v3.9) script (McGinness et al., 2025).
704 The script generated both Gaussian-fitted and raw distance datasets to verify accuracy
705 and consistency, from which average inter-peak distances and associated standard
706 deviations were computed. Kruskal–Wallis analysis was used to compare the median
707 peak distances among multiple groups. Post-hoc pairwise comparisons were performed
708 using Dunn's multiple comparison test with Bonferroni correction to identify specific
709 group differences.
710
711 **Histochemical staining of β-glucuronidase (GUS)**
712 GUS staining was performed as previously described (Li, 2011). Seedlings were
713 submerged in freshly prepared X-Gluc staining buffer containing 500 mM NaH_2PO_4, 500
714 mM $Na_2HPO_4 \cdot 7H_2O$, 1mM $K_3Fe(CN)_6$, 1 mM $K_4Fe(CN)_6$, 10 mM EDTA, 0.1% Triton
715 X-100, and 2.25 mM X-glucuronide (Cyrusbioscience), vacuumed for 20 min, and then
716 incubated at 37°C for 2−2.5 h. The pigments were washed out serially using 10−99%
717 ethanol for 30 min. Finally, the GUS staining was examined using a stereo microscope
718 (Prompt Ocean ST3E-0745 or Leica DM2500).
719
720 **Pi concentration and Pi uptake assays**

721 Pi concentrations were analysed as described (Ames, 1966) with minor modifications.
722 For the Pi assay, fresh tissue was homogenized with 1% glacial acetic acid and incubated
723 at 42℃ for 30 min, followed by centrifugation at 13,000×g for 5 min to obtain a clear
724 supernatant. The supernatant aliquot was mixed with the assay solution (0.35%
725 NH_4MoO_4, 0.86 N H_2SO_4, and 1.4% ascorbic acid) and incubated at 42℃ for an
726 additional 30 min before measurement at A_{750}. The Pi uptake assay for whole seedlings
727 was conducted in +P (250 μM KH_2PO_4) or −P (10 μM KH_2PO_4) medium supplemented
728 with ^{32}P as previously described (Kanno *et al.*, 2016).
729
730 **Total protein and microsomal protein extraction**
731 For the extraction of root total proteins, samples were ground in liquid N and dissolved
732 in protein lysis buffer containing 60 mM Tris-HCl (pH 8.5), 2% SDS, 2.5% glycerol, 0.13
733 mM EDTA, 1 mM phenylmethylsulfonyl fluoride (PMSF), and Protease Inhibitor
734 Cocktail (Sigma-Aldrich). Root microsomal proteins were extracted using the Minute™
735 Plant Microsomal Membrane Extraction Kit (Invent Biotechnologies) and were
736 resuspended in the same protein lysis buffer that was used for total protein extraction.
737
738 **Immunoblot analysis**
739 For *Arabidopsis* seedlings, a total of 25 μg of root total proteins or 15 μg of root
740 microsomal proteins from each sample were mixed with LDS sampling buffer containing
741 1 mM DTT. The mixture was then denatured by heating and loaded onto 4–12% Q-
742 PAGE™ Bis-Tris Precast Gel (SMOBIO) or NuPAGE 4–12% Bis-Tris Gels (Thermo
743 Fisher Scientific). For *N. benthamiana* leaves, 25 μg of total protein was used for loading.
744 Gel was transferred to polyvinylidene difluoride membranes (Immobilon-P Membrane or
745 Immobilon®-PSQ Membrane). Membrane was blocked with 1 or 2% BSA in 1× PBS
746 solution with 0.2% Tween 20 (PBST, pH 7.2) at RT for 1 h, and washed 4 times with 1×
747 PBST for 5 min followed by hybridization with primary antibodies of *At*PHT1;1/2/3
748 (1:1,000, PHY0753, PhytoAB), *At*PHT1;4 (Huang *et al.*, 2013), GFP (1:5,000, AS214696,
749 Agrisera) and S10 (1:1,000) for overnight at 4℃; *At*PHF1 (Huang *et al.*, 2013), *At*PHO1
750 (Liu *et al.*, 2012), and *At*CNIH5 (Liu *et al.*, 2024) at RT for 2 h. Anti-S10 polyclonal
751 rabbit antibody was raised against the peptide of S10 (MDLPDDHYLSTQTILSKDLN)
752 (Liu *et al.*, 2018) and produced by LTK BioLaboratories, Taiwan. Anti-*At*CNIH5

753 polyclonal rabbit antibody was raised and used as described (Liu *et al.*, 2024). The
754 membrane was washed four times with 1× PBST for 5 min, followed by hybridization
755 with the horseradish peroxidase–conjugated secondary antibody (1:20,000, GTX213110-
756 01 and 1:10,000, GTX213111-01, GeneTex) at RT for 1 h. After four washes in 1× PBST
757 for 5 min and a rinse with distilled water, chemiluminescent substrates (WesternBright
758 ECL and WesternBright Sirius ECL, Advansta) were applied for signal detection.
759
760 **Co-immunoprecipitation**
761 The root of 11-day-old *Arabidopsis UBQ10*: GFP and *AtCNIH5pro*: GFP-
762 *AtCNIH5/cnih5* complementation (COM) seedlings were grown under –P (0 μM
763 KH_2PO_4, seven days of starvation) conditions and ground in liquid nitrogen. The root
764 membrane fraction was isolated using the low-speed pellet (LSP) method as previously
765 described (Yoshimoto *et al.*, 2004) and resuspended in solubilization buffer containing
766 100 mM Tris-HCl (pH 7.5), 400 mM sucrose, 1 mM EDTA, 0.6% or 1% Triton X-100,
767 1 mM phenylmethylsulfonyl fluoride and Protease Inhibitor Cocktail (Sigma-Aldrich).
768 An equivalent of 30 μg or 100 μg of root membrane-enriched protein was loaded onto 5
769 μl of GFP-Trap beads (Chromotek) and incubated at 4°C for 2 h. The agarose beads were
770 then washed once with the abovementioned solubilization buffer containing 0.1% Triton
771 X-100 and resuspended in 1× Laemmli buffer. The mixture was boiled at 95°C for 5 min.
772 The centrifuged supernatant was collected for immunoblot analysis.
773
774 **Root growth analysis**
775 Seedlings were grown on +P (250 μM KH_2PO_4) or −P (10 μM KH_2PO_4) media. For
776 the measurement of primary and lateral root lengths on media containing 1.2% Bacto
777 agar, photos of roots were taken by a PowerShot G16 Camera (Canon), and the length
778 was measured using ImageJ segmented line function (Schneider *et al.*, 2012). Only lateral
779 roots with lengths longer than 2 mm were included for measurement. For the
780 measurement of root hair length, seedlings were grown on media containing 0.6% Bacto
781 agar. Root hairs were observed under the Leica DM2500 microscope equipped with DIC
782 optics and photographed. The ten longest root hairs within the maturation zone per root,
783 as defined from 5 mm to 10 mm away from the root tip, were measured by ImageJ. Root
784 hair numbers within the above-mentioned maturation zone were counted for root hair

785 density.
786
787 **Chemical treatments**
788 Acetosyringone (150 mM stock in DMSO; Sigma-Aldrich) and β-estradiol (36.7 mM
789 stock in ethanol; Sigma-Aldrich) were diluted to final concentrations of 150 μM and 36.7
790 μM, respectively, in ddH_2O.
791
792 **Accession Numbers**
793 Sequence data from this article can be found in the Arabidopsis Genome Initiative under
794 the following accession numbers: *At*CNIH1 (AT3G12180), *At*CNIH3 (AT1G62880),
795 *At*CNIH4 (AT1G12390), *At*CNIH5 (AT4G12090), *At*PHT1;1 (AT5G43350), *At*PHT1;4
796 (AT2G38940), *At*PHF1 (AT3G52190), *At*PHO1 (AT3G23430), *At*PHO2 (AT2G33770),
797 *At*SEC16A (AT5G47480), *At*SEC24A (AT3G07100), and *At*SAR1A (AT2G33120).
798
799 **Funding**
800 This work is supported by the Ministry of Science and Technology (MOST 108-2311-B-
801 007-003-MY3) and the National Science and Technology Council (NSTC 112-2313-B-
802 007-001-MY3).
803
804 **Acknowledgements**
805 We thank Prof. José A. Feijó at the University of Maryland, USA, for sharing the
806 *Arabidopsis cnih1/5* and *cnih3/5* mutants and plasmid encoding *35S*: RFP-*At*CNIH5. We
807 thank Dr. Tzyy-Jen Chiou at Academia Sinica, Taiwan (R.O.C.), for sharing the
808 *Arabidopsis phf1* mutants, anti-*At*PHT1;4, anti-*At*PHF1, and anti-*At*PHO1 antibodies. We
809 acknowledge Ms. Wen-Chun Chou for constructing the plasmid encoding *35S*: GFP1–10
810 and Mr. Po-Ruey Huang for cloning the NubG-*At*PHT1;4 construct. We acknowledge
811 Mr. Hong-Po Chen and Ms. Hui-Ying Chen for the genotyping of *phf1/cnih* mutants and
812 of *AtPHT1;1pro*: *At*PHT1;1-S11/*35S*: GFP1–10 in the WT and *cnih5* backgrounds and
813 the technical support from the confocal imaging core, National Tsing Hua University
814 (sponsored by MOST 108-2731-M-007-001 and MOST 110-2731-M-007-001). We are
815 grateful to Dr. Laurent Nussaume at CEA Cadarache, France, and Dr. Tzyy-Jen Chiou
816 for valuable comments on the manuscript.

Competing interests

None declared

Author contributions

T.-Y. L. conceived the project, designed, performed and analysed the experiments. C.-Y. C., C.-D. T., H.-F. L., J.-Y. W., M.-H. T., A. J. M., S. K., V. K. and C.-A. L. performed and analysed the experiments. T.-Y. L. and C.-Y. C. wrote the article.

Data availability

All data supporting the findings of this study are available within the article and the Supporting information (Figs S1–S14, Tabs S1–S2).

References

Ames, B. N. (1966) [10] Assay of inorganic phosphate, total phosphate and phosphatases. In: *Methods in enzymology.* Elsevier, pp. 115-118.

Ayadi, A., David, P., Arrighi, J.-F., Chiarenza, S., Thibaud, M.-C., Nussaume, L.*, et al.* (2015) Reducing the Genetic Redundancy of Arabidopsis PHOSPHATE TRANSPORTER1 Transporters to Study Phosphate Uptake and Signaling *Plant Physiology,* **167,** 1511-1526.

Bayle, V., Arrighi, J.-F., Creff, A., Nespoulous, C., Vialaret, J., Rossignol, M.*, et al.* (2011) Arabidopsis thaliana High-Affinity Phosphate Transporters Exhibit Multiple Levels of Posttranslational Regulation. *The Plant Cell,* **23,** 1523-1535.

Bökel, C., Dass, S., Wilsch-Bräuninger, M. and Roth, S. (2006) Drosophila Cornichon acts as cargo receptor for ER export of the TGFα-like growth factor Gurken. *Development,* **133,** 459-470.

Cardona-López, X., Cuyas, L., Marín, E., Rajulu, C., Irigoyen, M. L., Gil, E.*, et al.* (2015) ESCRT-III-associated protein ALIX mediates high-affinity phosphate transporter trafficking to maintain phosphate homeostasis in Arabidopsis. *The Plant Cell,* **27,** 2560-2581.

Chen, J., Wang, Y., Wang, F., Yang, J., Gao, M., Li, C.*, et al.* (2015) The Rice CK2 Kinase Regulates Trafficking of Phosphate Transporters in Response to Phosphate Levels. *The Plant Cell,* **27,** 711-723.

Clough, S. J. and Bent, A. F. (1998) Floral dip: a simplified method for Agrobacterium-mediated transformation of Arabidopsis thaliana. *The plant journal,* **16,** 735-743.

Delhaize, E. and Randall, P. J. (1995) Characterization of a phosphate-accumulator mutant of Arabidopsis thaliana. *Plant Physiology,* **107,** 207-213.

Gahoonia, T. S. and Nielsen, N. E. (1998) Direct evidence on participation of root hairs in phosphorus (32P) uptake from soil. *Plant and Soil,* **198,** 147-152.

Gangwar, S. P., Yen, L. Y., Yelshanskaya, M. V., Korman, A., Jones, D. R. and Sobolevsky, A. I. (2023) Modulation of GluA2–γ5 synaptic complex

858 desensitization, polyamine block and antiepileptic perampanel inhibition by
859 auxiliary subunit cornichon-2. *Nature structural & molecular biology,* **30,** 1481-
860 1494.
861 González, E., Solano, R., Rubio, V., Leyva, A. and Paz-Ares, J. (2005) PHOSPHATE
862 TRANSPORTER TRAFFIC FACILITATOR1 Is a Plant-Specific SEC12-
863 Related Protein That Enables the Endoplasmic Reticulum Exit of a High-Affinity
864 Phosphate Transporter in *Arabidopsis*. *The Plant Cell,* **17,** 3500-3512.
865 Harmel, N., Cokic, B., Zolles, G., Berkefeld, H., Mauric, V., Fakler, B.*, et al.* (2012)
866 AMPA receptors commandeer an ancient cargo exporter for use as an auxiliary
867 subunit for signaling. *PloS one,* **7,** e30681-e30681.
868 Herzig, Y., Sharpe, H. J., Elbaz, Y., Munro, S. and Schuldiner, M. (2012) A Systematic
869 Approach to Pair Secretory Cargo Receptors with Their Cargo Suggests a
870 Mechanism for Cargo Selection by Erv14. *PLOS Biology,* **10,** e1001329.
871 Huang, T.-K., Han, C.-L., Lin, S.-I., Chen, Y.-J., Tsai, Y.-C., Chen, Y.-R.*, et al.* (2013)
872 Identification of Downstream Components of Ubiquitin-Conjugating Enzyme
873 PHOSPHATE2 by Quantitative Membrane Proteomics in Arabidopsis Roots. *The*
874 *Plant Cell,* **25,** 4044-4060.
875 Jones Alexander, M., Xuan, Y., Xu, M., Wang, R.-S., Ho, C.-H., Lalonde, S.*, et al.* (2014)
876 Border Control—A Membrane-Linked Interactome of Arabidopsis. *Science,* **344,**
877 711-716.
878 Kanno, S., Arrighi, J.-F., Chiarenza, S., Bayle, V., Berthome, R., Peret, B.*, et al.* (2016)
879 A novel role for the root cap in phosphate uptake and homeostasis. *Elife,* **5,**
880 e14577.
881 Karthikeyan, A. S., Varadarajan, D. K., Mukatira, U. T., D'Urzo, M. P., Damsz, B. and
882 Raghothama, K. G. (2002) Regulated Expression of Arabidopsis Phosphate
883 Transporters. *Plant Physiology,* **130,** 221-233.
884 Lagunas-Gomez, D., Yañez-Dominguez, C., Zavala-Padilla, G., Barlowe, C. and Pantoja,
885 O. (2023) The C-terminus of the cargo receptor Erv14 affects COPII vesicle
886 formation and cargo delivery. *Journal of cell science,* **136,** jcs260527.
887 Lambers, H., Raven, J. A., Shaver, G. R. and Smith, S. E. (2008) Plant nutrient-
888 acquisition strategies change with soil age. *Trends in Ecology & Evolution,* **23,**
889 95-103.
890 Lapis-Gaza, H. R., Jost, R. and Finnegan, P. M. (2014) Arabidopsis PHOSPHATE
891 TRANSPORTER1 genes PHT1; 8 and PHT1; 9 are involved in root-to-shoot
892 translocation of orthophosphate. *BMC Plant Biology,* **14,** 1-19.
893 Lau, W.-T. W., Howson, R. W., Malkus, P., Schekman, R. and O'Shea, E. K. (2000)
894 Pho86p, an endoplasmic reticulum (ER) resident protein in Saccharomyces
895 cerevisiae, is required for ER exit of the high-affinity phosphate transporter
896 Pho84p. *Proceedings of the National Academy of Sciences,* **97,** 1107-1112.
897 Li, X. (2011) Histostaining for tissue expression pattern of promoter-driven GUS activity
898 in Arabidopsis. *Bio-protocol***,** e93-e93.
899 Liebminger, E., Huttner, S., Vavra, U., Fischl, R., Schoberer, J., Grass, J.*, et al.* (2009)
900 Class I α-mannosidases are required for N-glycan processing and root
901 development in Arabidopsis thaliana. *The Plant Cell,* **21,** 3850-3867.
902 Lin, W.-Y., Huang, T.-K. and Chiou, T.-J. (2013) Nitrogen limitation adaptation, a target
903 of microRNA827, mediates degradation of plasma membrane-localized
904 phosphate transporters to maintain phosphate homeostasis in Arabidopsis. *The*
905 *Plant cell,* **25,** 4061-4074.

Liu, T.-Y. (2021) Using Tripartite Split-sfGFP for the Study of Membrane Protein–Protein Interactions. In: *Arabidopsis Protocols.* (Sanchez-Serrano, J. J. and Salinas, J., eds.). New York, NY: Springer US, pp. 323-336.

Liu, T.-Y., Chou, W.-C., Chen, W.-Y., Chu, C.-Y., Dai, C.-Y. and Wu, P.-Y. (2018) Detection of membrane protein–protein interaction in planta based on dual-intein-coupled tripartite split-GFP association. *The Plant Journal,* **94,** 426-438.

Liu, T.-Y., Huang, T.-K., Tseng, C.-Y., Lai, Y.-S., Lin, S.-I., Lin, W.-Y*., et al.* (2012) PHO2-Dependent Degradation of PHO1 Modulates Phosphate Homeostasis in Arabidopsis *The Plant Cell,* **24,** 2168-2183.

Liu, T.-Y., Huang, T.-K., Yang, S.-Y., Hong, Y.-T., Huang, S.-M., Wang, F.-N*., et al.* (2016) Identification of plant vacuolar transporters mediating phosphate storage. *Nature Communications,* **7,** 11095.

Liu, T.-Y., Tsai, M.-H., Wang, J.-Y., Lung, H.-F., Chow, H.-X., Chiu, C.-Y*., et al.* (2024) CORNICHON HOMOLOG 5-dependent ER export of membrane cargoes in phosphate-starved Arabidopsis root as revealed by membrane proteomic analysis. *bioRxiv***,** 2024.2012.2030.630708.

Lung, H.-F., Chu, J.-D. and Liu, T.-Y. (2025) Involvement of PHOSPHATE TRANSPORTER TRAFFIC FACILITATOR1 in COPII assembly by interacting with SAR1 GTPase. *bioRxiv***,** 2025.2001. 2009.632146.

Manning, D. A. C. (2008) Phosphate Minerals, Environmental Pollution and Sustainable Agriculture. *Elements,* **4,** 105-108.

McGinness, A. J., Brooks, S. A., Strasser, R., Schoberer, J. and Kriechbaumer, V. (2025) Suborganellar resolution imaging for the localisation of human glycosylation enzymes in tobacco Golgi bodies. *Journal of Microscopy,* **297,** 258-273.

Misson, J., Thibaud, M.-C., Bechtold, N., Raghothama, K. and Nussaume, L. (2004) Transcriptional regulation and functional properties of Arabidopsis Pht1; 4, a high affinity transporter contributing greatly to phosphate uptake in phosphate deprived plants. *Plant molecular biology,* **55,** 727-741.

Młodzińska, E. and Zboińska, M. (2016) Phosphate Uptake and Allocation – A Closer Look at Arabidopsis thaliana L. and Oryza sativa L. *Frontiers in Plant Science,* **7**.

Mudge, S. R., Rae, A. L., Diatloff, E. and Smith, F. W. (2002) Expression analysis suggests novel roles for members of the Pht1 family of phosphate transporters in Arabidopsis. *The Plant Journal,* **31,** 341-353.

Müller, R., Morant, M., Jarmer, H., Nilsson, L. and Nielsen, T. H. (2007) Genome-Wide Analysis of the Arabidopsis Leaf Transcriptome Reveals Interaction of Phosphate and Sugar Metabolism. *Plant Physiology,* **143,** 156-171.

Nagarajan, V. K., Jain, A., Poling, M. D., Lewis, A. J., Raghothama, K. G. and Smith, A. P. (2011) Arabidopsis Pht1; 5 mobilizes phosphate between source and sink organs and influences the interaction between phosphate homeostasis and ethylene signaling. *Plant Physiology,* **156,** 1149-1163.

Nakagawa, T. (2019) Structures of the AMPA receptor in complex with its auxiliary subunit cornichon. *Science,* **366,** 1259-1263.

Nakanishi, H., Suda, Y. and Neiman, A. M. (2007) Erv14 family cargo receptors are necessary for ER exit during sporulation in Saccharomyces cerevisiae. *Journal of Cell Science,* **120,** 908-916.

Nelson, B. K., Cai, X. and Nebenführ, A. (2007) A multicolored set of in vivo organelle markers for co-localization studies in Arabidopsis and other plants. *The Plant*

954 *Journal,* **51,** 1126-1136.
955 Nussaume, L., Kanno, S., Javot, H., Marin, E., Nakanishi, T. M. and Thibaud, M.-C.
956 (2011) Phosphate Import in Plants: Focus on the PHT1 Transporters. *Frontiers in*
957 *Plant Science,* **2**.
958 Obrdlik, P., El-Bakkoury, M., Hamacher, T., Cappellaro, C., Vilarino, C., Fleischer, C.*,*
959 *et al.* (2004) K+ channel interactions detected by a genetic system optimized for
960 systematic studies of membrane protein interactions. *Proceedings of the National*
961 *Academy of Sciences of the United States of America,* **101,** 12242-12247.
962 Pagant, S., Wu, A., Edwards, S., Diehl, F. and Miller, Elizabeth A. (2015) Sec24 Is a
963 Coincidence Detector that Simultaneously Binds Two Signals to Drive ER
964 Export. *Current Biology,* **25,** 403-412.
965 Park, B. S., Seo, J. S. and Chua, N.-H. (2014) NITROGEN LIMITATION
966 ADAPTATION Recruits PHOSPHATE2 to Target the Phosphate Transporter
967 PT2 for Degradation during the Regulation of Arabidopsis Phosphate
968 Homeostasis. *The Plant Cell,* **26,** 454-464.
969 Poirier, Y. and Bucher, M. (2002) Phosphate Transport and Homeostasis in Arabidopsis.
970 *The Arabidopsis Book***,** e0024.
971 Powers, J. and Barlowe, C. (1998) Transport of Axl2p Depends on Erv14p, an ER–
972 Vesicle Protein Related to the Drosophila cornichon Gene Product. *The Journal*
973 *of Cell Biology,* **142,** 1209-1222.
974 Powers, J. and Barlowe, C. (2002) Erv14p Directs a Transmembrane Secretory Protein
975 into COPII-coated Transport Vesicles. *Molecular Biology of the Cell,* **13,** 880-
976 891.
977 Remy, E., Cabrito, T., Batista, R., Teixeira, M., Sá-Correia, I. and Duque, P. (2012) The
978 Pht1; 9 and Pht1; 8 transporters mediate inorganic phosphate acquisition by the
979 Arabidopsis thaliana root during phosphorus starvation. *New Phytologist,* **195,**
980 356-371.
981 Rosas-Santiago, P., Lagunas-Gómez, D., Barkla, B. J., Vera-Estrella, R., Lalonde, S.,
982 Jones, A.*, et al.* (2015) Identification of rice cornichon as a possible cargo receptor
983 for the Golgi-localized sodium transporter OsHKT1;3. *Journal of Experimental*
984 *Botany,* **66,** 2733-2748.
985 Roth, S., Shira Neuman-Silberberg, F., Barcelo, G. and Schüpbach, T. (1995) cornichon
986 and the EGF receptor signaling process are necessary for both anterior-posterior
987 and dorsal-ventral pattern formation in Drosophila. *Cell,* **81,** 967-978.
988 Schlücking, K., Edel, K. H., Köster, P., Drerup, M. M., Eckert, C., Steinhorst, L.*, et al.*
989 (2013) A new β-estradiol-inducible vector set that facilitates easy construction
990 and efficient expression of transgenes reveals CBL3-dependent cytoplasm to
991 tonoplast translocation of CIPK5. *Molecular plant,* **6,** 1814-1829.
992 Schneider, C. A., Rasband, W. S. and Eliceiri, K. W. (2012) NIH Image to ImageJ: 25
993 years of image analysis. *Nature Methods,* **9,** 671-675.
994 Shahan, R., Hsu, C.-W., Nolan, T. M., Cole, B. J., Taylor, I. W., Greenstreet, L.*, et al.*
995 (2022) A single-cell Arabidopsis root atlas reveals developmental trajectories in
996 wild-type and cell identity mutants. *Developmental Cell,* **57,** 543-560.e549.
997 Shin, H., Shin, H.-S., Dewbre, G. R. and Harrison, M. J. (2004) Phosphate transport in
998 Arabidopsis: Pht1;1 and Pht1;4 play a major role in phosphate acquisition from
999 both low- and high-phosphate environments. *The Plant Journal,* **39,** 629-642.
1000 Spitzer, M., Wildenhain, J., Rappsilber, J. and Tyers, M. (2014) BoxPlotR: a web tool for
1001 generation of box plots. *Nature methods,* **11,** 121-122.

1002 Takagi, J., Renna, L., Takahashi, H., Koumoto, Y., Tamura, K., Stefano, G., *et al.* (2013)
1003 MAIGO5 Functions in Protein Export from Golgi-Associated Endoplasmic
1004 Reticulum Exit Sites in Arabidopsis *The Plant Cell,* **25,** 4658-4675.
1005 Tanaka, N., Kato, M., Tomioka, R., Kurata, R., Fukao, Y., Aoyama, T., *et al.* (2014)
1006 Characteristics of a root hair-less line of Arabidopsis thaliana under physiological
1007 stresses. *Journal of Experimental Botany,* **65,** 1497-1512.
1008 Trevor, M. N., Nemanja, V., Che-Wei, H., Jingyuan, Z., Isabelle, V., Rachel, S., *et al.*
1009 (2022) Brassinosteroid gene regulatory networks at cellular resolution. *bioRxiv*,
1010 2022.2009.2016.508001.
1011 Wei, L., Liu, L., Chen, Z., Huang, Y., Yang, L., Wang, P., *et al.* (2023) CmCNIH1
1012 improves salt tolerance by influencing the trafficking of CmHKT1;1 in pumpkin.
1013 *The Plant Journal,* **114,** 1353-1368.
1014 Wudick, M. M., Portes, M. T., Michard, E., Rosas-Santiago, P., Lizzio, M. A., Nunes, C.
1015 O., *et al.* (2018) CORNICHON sorting and regulation of GLR channels underlie
1016 pollen tube Ca2+ homeostasis. *Science,* **360,** 533-536.
1017 Yáñez-Domínguez, C., Lagunas-Gómez, D., Torres-Cifuentes, D. M., Bezanilla, M. and
1018 Pantoja, O. (2023) A cornichon protein controls polar localization of the PINA
1019 auxin transporter in Physcomitrium patens. *Development,* **150,** dev201635.
1020 Yang, Z., Yang, J., Wang, Y., Wang, F., Mao, W., He, Q., *et al.* (2020) PROTEIN
1021 PHOSPHATASE95 Regulates Phosphate Homeostasis by Affecting Phosphate
1022 Transporter Trafficking in Rice. *The Plant Cell,* **32,** 740.
1023 Yoshimoto, K., Hanaoka, H., Sato, S., Kato, T., Tabata, S., Noda, T., *et al.* (2004)
1024 Processing of ATG8s, ubiquitin-like proteins, and their deconjugation by ATG4s
1025 are essential for plant autophagy. *The Plant cell,* **16,** 2967-2983.
1026 Zhang, D., Watson, J. F., Matthews, P. M., Cais, O. and Greger, I. H. (2021) Gating and
1027 modulation of a hetero-octameric AMPA glutamate receptor. *Nature,* **594,** 454-
1028 458.
1029 Zimmermannová, O., Felcmanová, K., Rosas-Santiago, P., Papoušková, K., Pantoja, O.
1030 and Sychrová, H. (2019) Erv14 cargo receptor participates in regulation of
1031 plasma-membrane potential, intracellular pH and potassium homeostasis via its
1032 interaction with K+-specific transporters Trk1 and Tok1. *Biochimica et*
1033 *Biophysica Acta (BBA) - Molecular Cell Research,* **1866,** 1376-1388.

1034

1035 **Supporting information**

1036 **Fig. S1** Expression of *AtCNIH* genes under Pi deprivation by RNA-seq analysis.
1037 Expression of *AtCNIH1/2/3/4/5* in the shoot and root of 10-day-old WT (Col-0) seedlings
1038 under Pi-sufficient conditions (+P0) or under one day (–P1) and three days of Pi starvation
1039 (–P3) as previously described (Liu *et al.*, 2016). RPKM stands for reads *per* kilobase of
1040 transcript *per* million mapped reads. Numbers represent average RPKM values of two
1041 replicates, with an assigned value of 0.25 for readings below this threshold.

1042

1043 **Fig. S2** Expression of *AtCNIH1pro:* GUS, *AtCNIH3pro:* GUS and *AtCNIH4pro:* GUS in
1044 *Arabidopsis*. (A, B) Expression of *AtCNIH1pro*: GUS, *AtCNIH3pro*: GUS, and

1045 *AtCNIH4pro*: GUS in the primary (A) and lateral roots (B) of 7-day-old *Arabidopsis*
1046 seedlings grown under +P (250 μM KH_2PO_4 and 7.5 mM KNO_3), –P (0 μM KH_2PO_4 and
1047 7.5 mM KNO_3, five days of starvation), or –N (250 μM KH_2PO_4 and 0.1 mM KNO_3, five
1048 days of starvation) conditions. Representative images are shown from three independent
1049 T3 homozygous lines. Scale bars, 100 μm.
1050
1051 **Fig. S3** Expression of *AtCNIH5pro:* GFP in *Arabidopsis*. Expression of *AtCNIH5pro*:
1052 GFP in 5-day-old *Arabidopsis* seedlings grown under +P (250 μM KH_2PO_4) or –P (0 μM
1053 KH_2PO_4, five days of starvation) conditions. The maturation zone, basal meristem, and
1054 apical meristem of the primary root are shown as indicated. Merged, single confocal
1055 sliced images of the green fluorescence and bright-field channels are shown.
1056 Representative images are shown from three independent T3 homozygous lines. Scale
1057 bars, 50 μm.
1058
1059 **Fig. S4** Complementation of *cnih5* by the expression of the genomic *AtCNIH5* and GFP-
1060 *AtCNIH5* sequences. (A–B) The shoot fresh weight (FW), Pi content, and Pi level of 11-
1061 day-old seedlings of *Arabidopsis* WT, *cnih5*, and *AtCNIH5pro*: GFP-*AtCNIH5/cnih5*
1062 complementation (COM) lines (A) or *AtCNIH5pro*: *AtCNIH5/cnih5* COM lines (B)
1063 grown under +P (250 μM KH_2PO_4) conditions. Error bar represents SE (n = 7 or 9 pools
1064 of seedings from independent experiments). One-way ANOVA with post-hoc Dunnett's
1065 test versus *cnih5,* $^{*}p < 0.05$, $^{**}p < 0.01$. (C) Protein expression of *At*PHT1;1/2/3, *AtCNIH5*,
1066 or GFP-*AtCNIH5* in the low-speed pellet (LSP) of *Arabidopsis* WT, *cnih5,* and COM
1067 lines under –P (0 μM KH_2PO_4, three days of starvation) conditions. The relative
1068 expression level was normalized with the corresponding amido black staining and relative
1069 to the WT control. One representative immunoblot from two independent experiments is
1070 shown, and quantitative data are indicated as mean ± SE (n = 2) for the relative expression
1071 of *At*PHT1;1/2/3. Root microsomal protein was isolated by the LSP method as previously
1072 described (Yoshimoto *et al.*, 2004).
1073
1074 **Fig. S5** The expression of Pi starvation-induced genes and the root phenotypes of
1075 *Arabidopsis cnih5.* (A) RT-qPCR analysis of the transcript expression of *AtPHT1;1–1;4*,
1076 *AtACP5*, and *AtPHF1* in the root of 11-day-old *Arabidopsis* WT and *cnih5* seedlings

1077 grown under +P (250 μM KH_2PO_4) or –P (0 μM KH_2PO_4, three days of starvation)
1078 conditions. (B, C) The primary root (PR) length (B) and the lateral root (LR) density (C)
1079 of 9-day-old *Arabidopsis* WT and *cnih5* seedlings grown under +P (250 μM KH_2PO_4) or
1080 –P (10 μM KH_2PO_4, five days of starvation) conditions. (D–F) The shoot Pi level (D),
1081 the root hair (RH) length (E), and the RH density (F) of 5-day-old *Arabidopsis* WT and
1082 *cnih5* seedlings grown under +P (250 μM KH_2PO_4) or –P (10 μM KH_2PO_4, three days of
1083 starvation in D, E or 0 μM KH_2PO_4, five days of starvation in F). Data in (B, C, E, and
1084 F) are visualized using BoxPlotR (Spitzer *et al.*, 2014). Data points are plotted as dots.
1085 The number of dots is indicated at the bottom of each figure. The centre lines show the
1086 medians; the central plus signs (+) show the means; box limits indicate the 25th and 75th
1087 percentiles; whiskers extend to the minimum and the maximum values. Error bar
1088 represents SE in D (n = 3, pools of seedlings from independent experiments). Data
1089 significantly different from the corresponding WT in (D) are indicated by asterisks ($^*p <$
1090 0.05; Student's t-test, two-tailed) and from the other groups in (B), (C), (E), and (F) are
1091 indicated by different lowercase letters (Two-Way ANOVA, Duncan's test).
1092
1093 **Fig. S6** Decreased *At*PHT1s and increased *At*PHF1 in the total root proteins from
1094 *Arabidopsis cnih5*. Protein expression of *At*PHT1;1/2/3, *At*PHT1;4 and *At*PHF1 in the
1095 root of 11-day-old seedlings of *Arabidopsis* WT, *cnih4,* and *cnih5* under +P (250 μM
1096 KH_2PO_4) or –P (0 μM KH_2PO_4, three days of starvation) conditions. The relative
1097 expression level of *At*PHT1;1/2/3, *At*PHT1;4, and *At*PHF1 was normalized with the
1098 corresponding actin and relative to the WT control. Error bars represent SE (n = 3–4,
1099 pools of seedlings from independent experiments). One-way ANOVA with post-hoc
1100 Dunnett's test versus WT, $^*p < 0.05$.
1101
1102 **Fig. S7** Analyses of *Arabidopsis cnih1/5, cnih3/5*, and *cnih4/5* seedlings. (A) The
1103 transcript expression of *AtCNIH* genes in the root of 11-day-old *Arabidopsis* WT, *cnih5*,
1104 *cnih1/5*, *cnih3/5*, and *cnih4/5* seedlings grown under +P (250 μM KH_2PO_4) conditions
1105 assessed by RT-qPCR or RT-PCR. (B, C) The shoot and root fresh weight (FW) (B) and
1106 Pi levels (C) of 11-day-old *Arabidopsis* WT, *cnih5*, *cnih1/5*, *cnih3/5*, and *cnih4/5*
1107 seedlings grown under +P (250 μM KH_2PO_4) or –P (0 μM KH_2PO_4, three days of
1108 starvation) conditions. Error bars represent SE (n = 6–10, pools of seedlings from

1109 independent experiments). One-way ANOVA with post-hoc Dunnett's test versus *cnih5*,
1110 $^{*}p < 0.05$.
1111
1112 **Fig. S8** Phenotypes of *Arabidopsis phf1, phf1/cnih4, phf1/cnih5*, and *phf1/cnih4/5* adult
1113 plants. (A, B) The shoot and root fresh weight (FW) (A) and Pi levels (B) of 20-day-old
1114 *Arabidopsis* WT, *phf1*, *phf1/cnih*4, *phf1/cnih5*, and *phf1/cnih4/5* plants grown under +P
1115 (250 μM KH_2PO_4) or –P (10 μM KH_2PO_4, five days of starvation) hydroponic conditions.
1116 Data are visualized using BoxPlotR (Spitzer *et al.*, 2014). Centre lines show the medians;
1117 the central plus signs (+) show the means; box limits indicate the 25th and 75th
1118 percentiles; whiskers extend to the 5th and 95th percentiles, and data points are plotted
1119 as dots. Data significantly different from the other groups are indicated by different
1120 lowercase letters (n = 15–24, biological replicates from independent experiments; One-
1121 Way ANOVA, Duncan's test).
1122
1123 **Fig. S9** *At*PHO2 does not mediate the degradation of *At*CNIH5. (A) Co-expression of
1124 S10-*At*CNIH5 with the catalytically defective *At*PHO2^{C748A}-S11 in the presence of
1125 GFP1–9 in *N. benthamiana* leaves. Images are from single confocal slices. Scale bars, 20
1126 μm. The co-expression of S10-*At*CNIH5 with *At*PHT1;1-S11 and S10-3xHA-S11 are,
1127 respectively, used as positive and negative protein–protein interaction controls. (B)
1128 Immunoblot analysis of S10-*At*CNIH5 and S10-*At*PHO1 in *N. benthamiana* leaves under
1129 co-expression of increasing levels of S10-*At*PHO2. The co-expression of GFP is used as
1130 a negative control. Anti-S10 antibodies also detect free GFP.
1131
1132 **Fig. S10** Interaction analysis of *At*PHT1;1 and *At*PHF1 with *At*CNIH1, *At*CNIH3, and
1133 *At*CNIH4. (A, B) Co-expression of *At*PHT1;1-PLVCub (A) and *At*PHF1-PLVCub (B)
1134 with NubG-*At*CNIH1, -*At*CNIH3, or -*At*CNIH4 in the yeast split-ubiquitin system. The
1135 co-expression of *At*PHT1;1-PLVCub or *At*PHF1-PLVCub with NubI and NubG are used
1136 as positive and negative controls, respectively. Yeast transformants were grown on
1137 synthetic medium without leucine and tryptophan (–LW; the left panel) or on synthetic
1138 medium lacking leucine, tryptophan, adenine, and histidine-containing 0.5 μM
1139 methionine (–LWAH; middle panel) or on SC–LW containing 2 mg/L X-gal (X-gal; the
1140 right panel).

1141

1142 **Fig. S11** The CORNICHON-RELATED family (PTHR12290) in Protein Analysis
1143 THrough Evolutionary Relationships (PANTHER). Green circles represent speciation
1144 events, while orange circles represent duplication. Diamonds are expanded subfamily
1145 nodes, and triangles are collapsed nodes. Note that we have collapsed some nodes (shown
1146 with triangles) here to simplify the diagram by hiding some descendant subtrees.
1147 Different colors correspond to different subfamilies. The whole family tree can be
1148 explored at www.pantherdb.org/treeViewer/treeViewer.jsp?book= PTHR12290

1149

1150 **Fig. S12** Impaired plasma membrane targeting of *At*PHT1;1-S11 in *Arabidopsis phf1*.
1151 Representative images of localization of *At*PHT1;1-S11 in 5-day-old *AtPHT1;1pro*:
1152 *At*PHT1;1-S11/*35S*: GFP1–10 seedlings grown under −P (0 μM KH_2PO_4) conditions.
1153 Independent lines in the *phf1* and *cnih5* backgrounds, and the corresponding WT controls
1154 are used for comparison. Arrows indicate GFP signals surrounding the nuclear
1155 membrane. RAM, Root apical meristem; TZ, transition zone; EZ, elongation zone; DZ,
1156 differentiation zone. Images are from single confocal slices. Scale bar, 20 μm.

1157

1158 **Fig. S13** Expression of *AtPHT1;1*, *AtPHT1;2*, *AtPHT1;4*, *AtPHT1;5*, *AtPHT1;7–1;9*,
1159 *AtCNIH1–5,* and *AtPHF1* revealed by single-cell mRNA sequencing (scRNA-seq) of
1160 *Arabidopsis* root. The dot plot used to visualize single-cell gene expression in
1161 *Arabidopsis* roots is retrieved from ARVEX (https://shiny.mdc-berlin.de/ARVEX/),
1162 which hosts processed scRNA-seq data of wild-type samples from Shahan *et al.* (2022)
1163 and Trevor *et al.* (2023). PctExp: Percentage of cells expressing the gene in a specific
1164 time zone and cell type; circle size represents the proportion (%) of cells expressing a
1165 given gene. AvgExp: Averaged normalized gene expression value in a specific time zone
1166 and cell type; the colour of the scale bar represents the mean expression (natural log +1
1167 pseudocount).

1168

1169 **Fig. S14** Schematic representations of *AtCNIH* gene promoter-fused GUS and GFP
1170 reporter constructs. Schematic representations of *AtCNIH1*, *AtCNIH3*, *AtCNIH4*, and
1171 *AtCNIH5* promoter-fused GUS reporter constructs (A) and *AtCNIH5* promoter-fused
1172 GFP reporter construct (B). The upstream region of transcription started site (TSS) in

1173 *AtCNIH* genes was shown by a white arrow, and gray boxes showed the 5' untranslated
1174 regions.
1175
1176 **Table S1.** Oligonucleotides used for PCR genotyping, RT-PCR, and RT-qPCR analyses.
1177 **Table S2.** Oligonucleotides used for plasmid constructs.
1178
1179 **Figure legends**
1180 **Fig. 1** Pi starvation-induced expression pattern of *At*CNIH5. (A) RT-qPCR analysis of *A.*
1181 *thaliana CNIH1, CNIH3, CNIH4,* and *CNIH5* in the shoot and root of 11-day-old
1182 seedlings grown under +P+N (250 μM KH_2PO_4 and 7.5 mM KNO_3), –P+N (0 μM
1183 KH_2PO_4 and 7.5 mM KNO_3, three days of starvation), or +P–N (250 μM KH_2PO_4 and 0
1184 μM KNO_3, three days of starvation) conditions. Relative gene expression is presented as
1185 fold change compared to the control under +P+N conditions. Error bars represent SE (n
1186 = 4, pools of seedings from independent experiments). Dunn's test following Kruskal–
1187 Wallis test, $*p < 0.05$. (B) Expression of *AtCNIH5pro*: GUS in 7-day-old seedlings grown
1188 under +P (250 μM KH_2PO_4) or –P (0 μM KH_2PO_4, five days of starvation) conditions. i–
1189 vi (+P; shoot part; trichome; primary root tip; primary root maturation zone; lateral root
1190 tip; lateral root maturation zone). vii–x (–P; primary root tip; primary root maturation
1191 zone; lateral root tip; lateral root maturation zone). Scale bars, 10 mm in i, 0.1 mm in ii,
1192 and 100 μm in iii–x. Representative images are shown from three independent T3
1193 homozygous lines.
1194
1195 **Fig. 2** Subcellular localization of *At*CNIH5 to the ER and ERES. (A) The ER and ERES
1196 localizations of S10-*At*CNIH5 in agro-infiltrated *N. benthamiana* leaves. mCherry-
1197 HDEL, luminal ER marker; *At*SEC16A-S11, ERES marker. Images are from single
1198 confocal slices. Scale bars, 10 μm. (B, C) Statistical line profile analysis of fluorescence
1199 intensity for localization of *At*CNIH5 with the ERES and *cis*-Golgi markers.
1200 Representative images and line profile analysis for *35S:* RFP-*At*CNIH5 (B) and
1201 *UBQ10*:*sXVE*: mCherry-*At*CNIH5 (C) (magenta) with the *cis*-Golgi marker MNS1-eGFP
1202 and the ERES markers *At*SAR1A-GFP, GFP-*At*SEC16A, and GFP-*At*SEC24A (green).
1203 The line profile applied and the line profile output are shown. Peak distance analysis
1204 graphs showing the co-localization analysis with RFP-*At*CNIH5 and mCherry-*At*CNIH5

1205 with the ERES and *cis*-Golgi markers. Scale bars = 1 μm. Kruskal–Wallis analysis was
1206 used to compare the median peak distances among multiple groups. Post-hoc pairwise
1207 comparisons were performed using Dunn's multiple comparison test with Bonferroni
1208 correction to identify significant group differences ($^{***}p < 0.001$). Error bars represent SE
1209 (n = 4 biological replicas, with at least 18 technical repeats). (D) Localization of GFP-
1210 *AtCNIH5* in the root of *Arabidopsis* 5-day-old seedlings grown under –P (0 μM KH_2PO_4,
1211 five days of starvation) conditions. TZ/EZ, transition zone/elongation zone; RH, root hair.
1212 Images are from single confocal slices. Scale bars, 10 μm.
1213
1214 **Fig. 3** *At*CNIH5 interacts with *At*PHT1;1, *At*PHT1;4, and *At*PHF1. (A) Expression of
1215 S10-*At*CNIH5, S10-*At*PHF1, S10-3xHA and *At*PHT1;1-S11 in the presence of S11-
1216 GFP1–9 or GFP1–9 in *N. benthamiana* leaves. The co-expression of *At*PHT1;1-S11 with
1217 S10-*At*PHF1 and S10-3xHA are used as positive and negative protein–protein interaction
1218 controls, respectively. Images are from single confocal slices. Scale bars, 10 μm. (B) Co-
1219 expression of PLVCub-*At*CNIH5 with NubG-*At*PHF1, NubG-*At*PHT1;1, and NubG-
1220 *At*PHT1;4 in the yeast split-ubiquitin system. The co-expression of PLVCub-*At*CNIH5
1221 with NubI and NubG are used as positive and negative controls, respectively. Yeast
1222 transformants were grown on synthetic medium without leucine and tryptophan (–LW;
1223 the left panel) or on synthetic medium lacking leucine, tryptophan, adenine, and histidine-
1224 containing 500 μM methionine (–LWAH; middle panel) or on SC–LW containing 2 mg/L
1225 X-gal (X-gal; the right panel). (C) Coimmunoprecipitation of *At*PHT1;1/2/3 and *At*PHF1
1226 with GFP-*AtCNIH5* in 11-day-old *AtCNIH5pro*: GFP-*AtCNIH5/cnih5* complementation
1227 (COM) seedlings grown under –P (0 μM KH_2PO_4, seven days of starvation) conditions.
1228 A *UBQ10*: GFP line was used as a control. The amount of root low-speed pellet (LSP)
1229 membrane fraction used for the input or the immunoprecipitation (IP) loading is shown
1230 as indicated. The relative abundance of co-immunoprecipitated endogenous
1231 *At*PHT1;1/2/3 and *At*PHF1 proteins was calculated by normalizing them with the GFP
1232 control. Data significantly different from the GFP control are indicated by asterisks (n =
1233 3 biological replicates; $^{*}p < 0.05$; Student's t-test, two-tailed).
1234
1235 **Fig. 4** Loss of *AtCNIH5* leads to decreased shoot Pi levels, lower abundance of *At*PHT1
1236 proteins, and diminished Pi uptake. (A, B) The shoot and root fresh weight (FW) (A) and

1237 Pi levels (B) of 11-day-old *Arabidopsis* WT and *cnih5* seedlings under +P (250 μM
1238 KH_2PO_4) or–P (0 μM KH_2PO_4, three days of starvation) conditions. Error bars represent
1239 SE (n = 15–16, pools of seedlings from independent experiments; $^{*}p < 0.05$, $^{**}p < 0.01$;
1240 Student's t-test, two-tailed). (C) Expression of *At*PHT1;1/2/3 and *At*PHT1;4 in the root
1241 microsomal fractions from 11-day-old *Arabidopsis* WT and *cnih5* seedlings under +P
1242 (250 μM KH_2PO_4) or –P (0 μM KH_2PO_4, three days of starvation) conditions. The relative
1243 expression levels of *At*PHT1;1/2/3 and *At*PHT1;4 were normalized with the
1244 corresponding amido black staining and relative to the WT control. Error bars represent
1245 SE (n = 2, pools of seedlings from independent experiments). (D) Quantification of Pi
1246 uptake and shoot-to-root distribution. Data are visualized using BoxPlotR (Spitzer *et al.*,
1247 2014). The centre lines show the medians; the central plus signs (+) show the means; box
1248 limits indicate the 25th and 75th percentiles; whiskers extend to the minimum and the
1249 maximum values. Data points are plotted as dots. Data significantly different from WT
1250 are indicated by asterisks (n = 8 biological replicates; $^{*}p < 0.05$, $^{**}p < 0.01$; Student's t-
1251 test, two-tailed).
1252
1253 **Fig. 5** Impaired plasma membrane targeting of split-GFP-tagged *At*PHT1;1 in *cnih5* root.
1254 (A) Reduction of *At*PHT1;1-S11 at the plasma membrane of the epidermal cells in the
1255 root transition/elongation zone of 5-day-old *cnih5* seedlings under −P (0 μM KH_2PO_4)
1256 conditions. The transgenic lines expressing *AtPHT1;1pro*: *At*PHT1;1-S11/*35S*: GFP1–10
1257 in the *cnih5* and corresponding WT backgrounds were used for comparison.
1258 Representative images and line-scan fluorescence intensity profiles (arbitrary unit, a.u.)
1259 of *At*PHT1;1-S11 are shown in the left panel. Arrows indicate the acropetal direction. The
1260 fluorescence intensity histogram of *At*PHT1;1-S11 enclosed by the representative
1261 rectangle is quantified in the right panel. Data significantly different from WT are
1262 indicated by asterisks (n, counted regions from transition/elongation zone of 8 roots; $^{**}p$
1263 < 0.01; Student's t-test, two-tailed). Scale bars, 20 μm. (B) A representative image shows
1264 increased intracellular retention of *At*PHT1;1-S11 in the root epidermal cells along the
1265 transition zone and the elongation zone of *cnih5*. Scale bars, 20 μm. (C) Reduction of
1266 *At*PHT1;1-S11 at the plasma membrane in the *cnih5* root hair. Line-scan profiles were
1267 performed at a distance of 30 μm from the root hair tip as indicated by the dashed line for
1268 quantification of PM fluorescence intensity (arbitrary unit, a.u.). All the fluorescence

1269 images are acquired from a single confocal optical slice. Quantitative data in the right
1270 panel are visualized using BoxPlotR (Spitzer *et al.*, 2014). The centre lines show the
1271 medians; the central plus signs (+) show the means; box limits indicate the 25th and 75th
1272 percentiles; whiskers extend to the smallest data point within 1.5 times the interquartile
1273 range from the lower and upper quartiles. Data significantly different from WT are
1274 indicated by asterisks (n, counted root hairs; $^{**}p < 0.01$; Student's t-test, two-tailed). Scale
1275 bars, 20 μm.
1276
1277 **Fig. 6** Loss of *AtCNIH5* exacerbates the growth retardation of *phf1*. (A, B) The shoot and
1278 root fresh weight (FW) (A) and Pi levels (B) of 11-day-old *Arabidopsis* WT, *phf1,*
1279 *phf1/cnih4, phf1/cnih5*, and *phf1/cnih4/5* seedlings grown under +P (250 μM KH_2PO_4)
1280 or –P (0 μM KH_2PO_4, three days of starvation) conditions. Error bars represent SE (n =
1281 7–8, pools of seedlings from independent experiments. (C) The expression of
1282 *At*PHT1;1/2/3 in the root of 11-day-old *Arabidopsis* WT, *phf1, phf1/cnih4, phf1/cnih5*,
1283 and *phf1/cnih4/5* seedlings grown under +P (250 μM KH_2PO_4) or –P (0 μM KH_2PO_4,
1284 three days of starvation) conditions. The relative expression level of *At*PHT1;1/2/3 was
1285 normalized with the corresponding actin and relative to the WT control. Error bars
1286 represent SE (n = 3, pools of seedlings from independent experiments). One-way
1287 ANOVA with post-hoc Dunnett's test versus *phf1,* $^{*}p < 0.05$, $^{**}p < 0.01$.
1288
1289 **Fig. 7** Loss of *AtCNIH5* suppresses Pi accumulation in *Arabidopsis pho2*. (A, B) The
1290 shoot Pi level (A) and the expression of *At*PHT1;1/2/3, *At*PHT1;4, and *At*PHO1 in the
1291 root (B) of 11-day-old *Arabidopsis* WT, *pho2,* and *cnih5/pho2* seedlings grown under +P
1292 (250 μM KH_2PO_4) conditions. Error bars represent SE (n = 5–7, pools of seedlings from
1293 independent experiments One-way ANOVA with post-hoc Dunnett's test versus *pho2,*
1294 $^{**}p < 0.01$. One representative immunoblot from two independent experiments is shown.
1295
1296 **Fig. 8** A working model of *At*CNIH5-mediated ER exit of *At*PHT1s. In *Arabidopsis*,
1297 *PHF1* and *CNIH5* are expressed at distinct and overlapping root developmental zones
1298 (left panel). In the non-dividing epidermal cell (right panel), including the transition
1299 zone/elongation zone and the root hair cell of the differentiation zone, the transcripts of
1300 *PHT1* genes, *PHF1*, and *CNIH5* are increased under Pi starvation (−P). CNIH5 interplays

1301 with PHF1 to facilitate the ER exit and the plasma membrane (PM) targeting of PHT1s
1302 in a COPII-dependent manner. While PHF1 may interact with PHT1s that are competent
1303 for the ER exit at an upstream step of COPII recruitment, CNIH5 may selectively mediate
1304 the efficient incorporation of PHT1s into the COPII vesicle delivered to the Golgi. CNIH5
1305 may also act as a cargo receptor for other membrane proteins. RAM, root apical meristem;
1306 TZ, transition zone; EZ, elongation zone; DZ, differentiation zone.
1307
1308 **Table 1.** Intracellular retention of split-GFP tagged-*At*PHT1;1 in the root
1309 transition/elongation zones of *cnih5*.

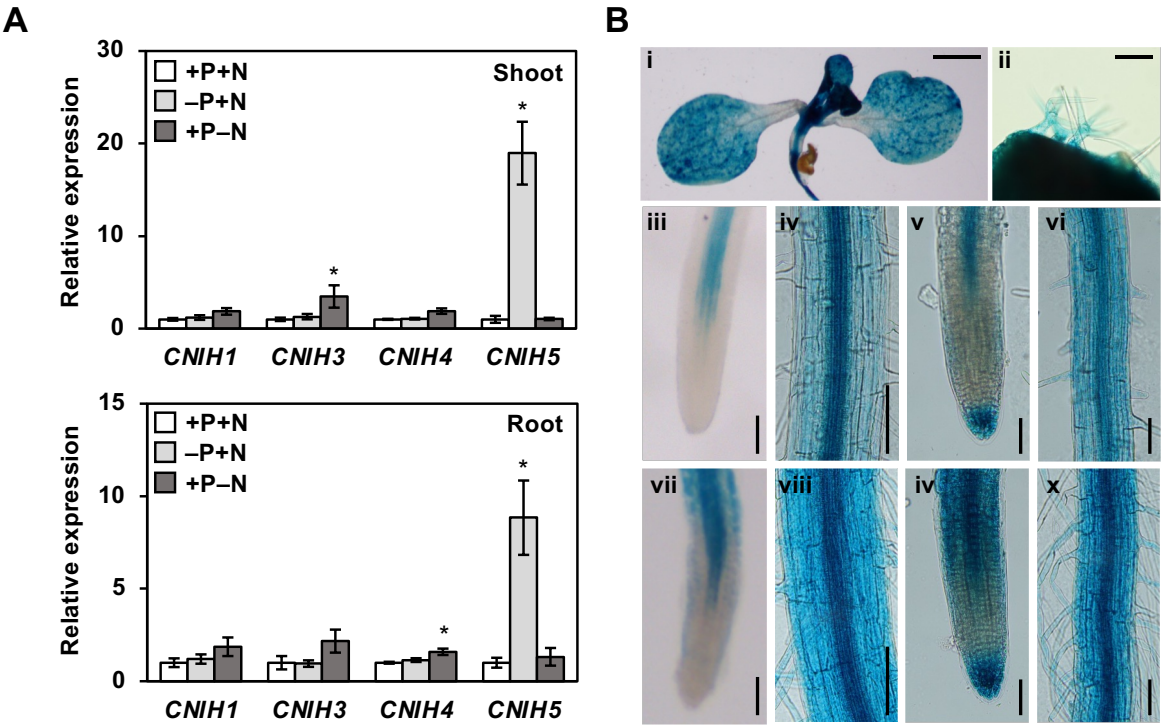

Fig. 1 Pi starvation-induced expression pattern of *At*CNIH5. (A) RT-qPCR analysis of *A. thaliana CNIH1, CNIH3, CNIH4,* and *CNIH5* in the shoot and root of 11-day-old seedlings grown under +P+N (250 µM KH_2PO_4 and 7.5 mM KNO_3), –P+N (0 µM KH_2PO_4 and 7.5 mM KNO_3, three days of starvation), or +P–N (250 µM KH_2PO_4 and 0 µM KNO_3, three days of starvation) conditions. Relative gene expression is presented as fold change compared to the control under +P+N conditions. Error bars represent SE (n = 4, pools of seedings from independent experiments). Dunn's test following Kruskal–Wallis test, $*p < 0.05$. (B) Expression of *AtCNIH5pro*: GUS in 7-day-old seedlings grown under +P (250 µM KH_2PO_4) or –P (0 µM KH_2PO_4, five days of starvation) conditions. i–vi (+P; shoot part; trichome; primary root tip; primary root maturation zone; lateral root tip; lateral root maturation zone). vii–x (–P; primary root tip; primary root maturation zone; lateral root tip; lateral root maturation zone). Scale bars, 10 mm in i, 0.1 mm in ii, and 100 µm in iii–x. Representative images are shown from three independent T3 homozygous lines.

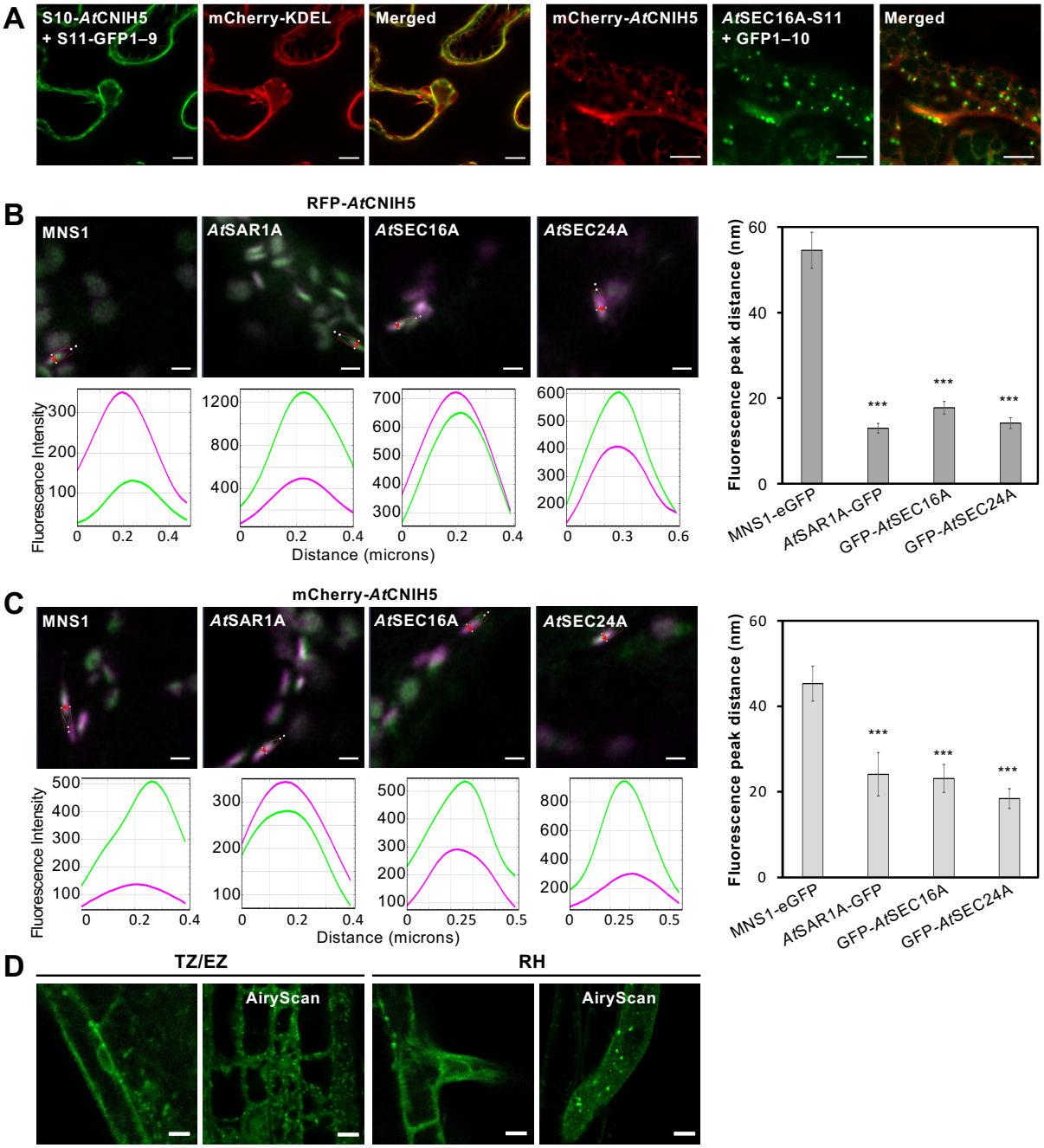

Fig. 2 Subcellular localization of *At*CNIH5 to the ER and ERES. (A) The ER and ERES localizations of S10-*At*CNIH5 in agro-infiltrated *N. benthamiana* leaves. mCherry-HDEL, luminal ER marker; *At*SEC16A-S11, ERES marker. Images are from single confocal slices. Scale bars, 10 µm. (B, C) Statistical line profile analysis of fluorescence intensity for localization of *At*CNIH5 with the ERES and *cis*-Golgi markers. Representative images and line profile analysis for *35S:* RFP-*At*CNIH5 (B) and *UBQ10*:*sXVE*: mCherry-*At*CNIH5 (C) (magenta) with the *cis*-Golgi marker MNS1-eGFP and the ERES markers *At*SAR1A-GFP, GFP-*At*SEC16A, and GFP-*At*SEC24A (green). The line profile applied and the line profile output are shown. Peak distance analysis graphs showing the co-localization analysis with RFP-*At*CNIH5 and mCherry-*At*CNIH5 with the ERES and *cis*-Golgi markers. Scale bars = 1 µm. Kruskal–Wallis analysis was used to compare the median peak distances among multiple groups. Post-hoc pairwise comparisons were performed using Dunn's multiple comparison test with Bonferroni correction to identify significant group differences ($^{***}p < 0.001$). Error bars represent SE (n = 4 biological replicas, with at least 18 technical repeats). (D) Localization of GFP-*AtCNIH5* in the root of *Arabidopsis* 5-day-old seedlings grown under –P (0 µM KH_2PO_4, five days of starvation) conditions. TZ/EZ, transition zone/elongation zone; RH, root hair. Images are from single confocal slices. Scale bars, 10 µm.

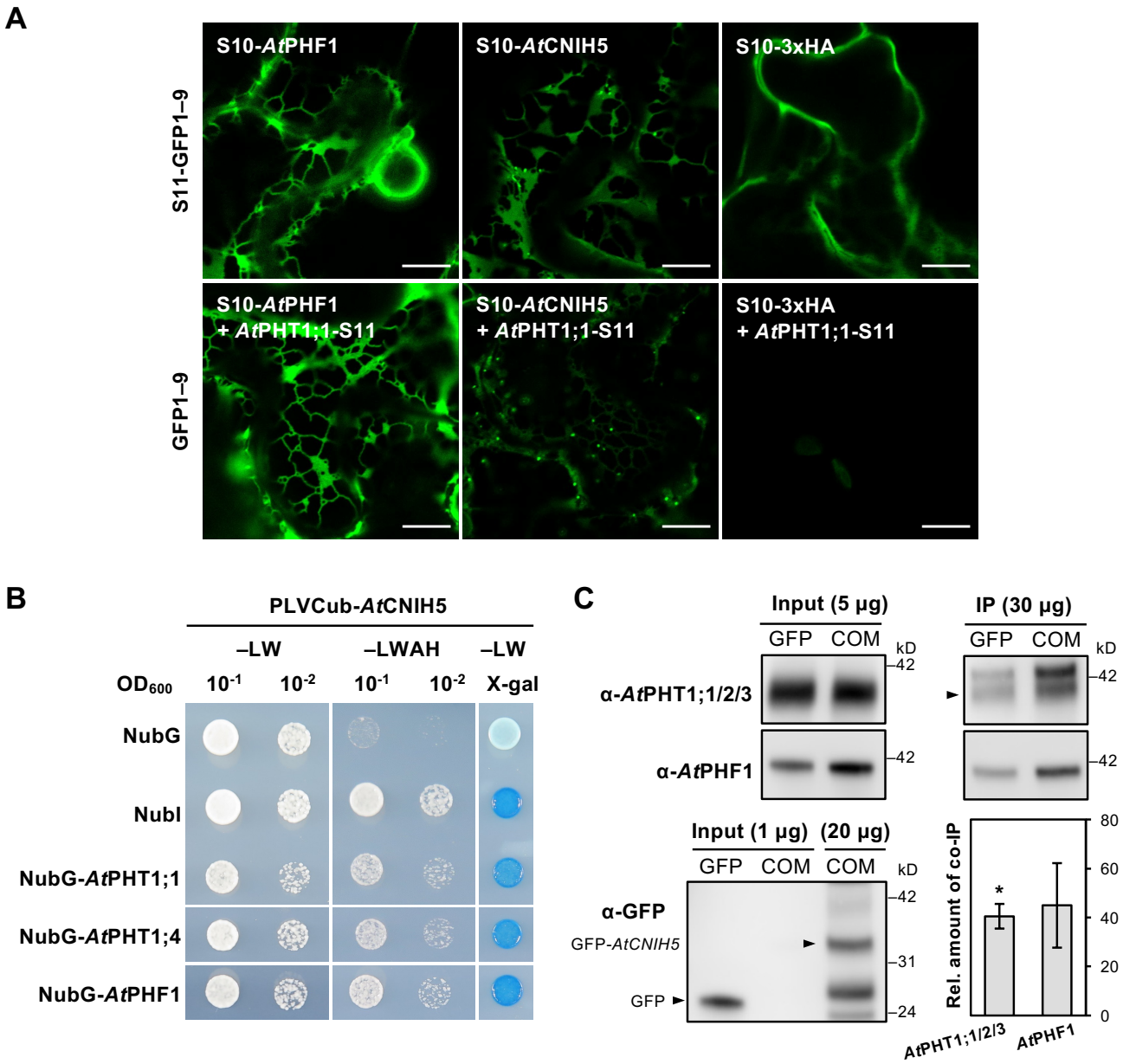

Fig. 3 *At*CNIH5 interacts with *At*PHT1;1, *At*PHT1;4, and *At*PHF1. (A) Expression of S10-*At*CNIH5, S10-*At*PHF1, S10-3xHA and *At*PHT1;1-S11 in the presence of S11-GFP1–9 or GFP1–9 in *N. benthamiana* leaves. The co-expression of *At*PHT1;1-S11 with S10-*At*PHF1 and S10-3xHA are used as positive and negative protein–protein interaction controls, respectively. Images are from single confocal slices. Scale bars, 10 µm. (B) Co-expression of PLVCub-*At*CNIH5 with NubG-*At*PHF1, NubG-*At*PHT1;1, and NubG-*At*PHT1;4 in the yeast split-ubiquitin system. The co-expression of PLVCub-*At*CNIH5 with NubI and NubG are used as positive and negative controls, respectively. Yeast transformants were grown on synthetic medium without leucine and tryptophan (–LW; the left panel) or on synthetic medium lacking leucine, tryptophan, adenine, and histidine-containing 500 µM methionine (–LWAH; middle panel) or on SC–LW containing 2 mg/L X-gal (X-gal; the right panel). (C) Coimmunoprecipitation of *At*PHT1;1/2/3 and *At*PHF1 with GFP-*AtCNIH5* in 11-day-old *AtCNIH5pro*: GFP-*AtCNIH5/cnih5* complementation (COM) seedlings grown under –P (0 µM KH_2PO_4, seven days of starvation) conditions. A *UBQ10*: GFP line was used as a control. The amount of root low-speed pellet (LSP) membrane fraction used for the input or the immunoprecipitation (IP) loading is shown as indicated. The relative abundance of co-immunoprecipitated endogenous *At*PHT1;1/2/3 and *At*PHF1 proteins was calculated by normalizing them with the GFP control. Data significantly different from the GFP control are indicated by asterisks (n = 3 biological replicates; $^{*}p < 0.05$; Student's t-test, two-tailed).

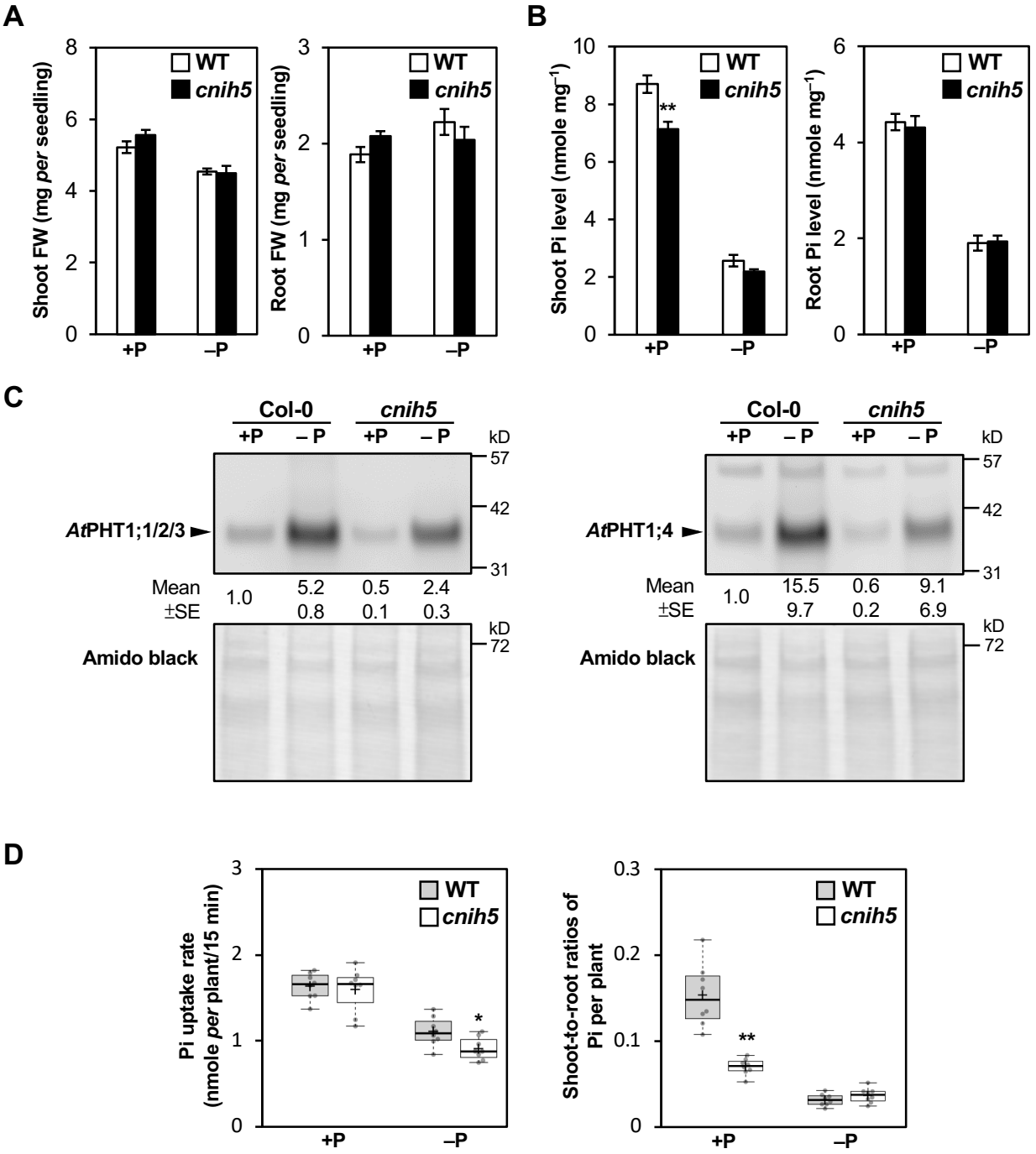

Fig. 4 Loss of *AtCNIH5* leads to decreased shoot Pi levels, lower abundance of *At*PHT1 proteins, and diminished Pi uptake. (A, B) The shoot and root fresh weight (FW) (A) and Pi levels (B) of 11-day-old *Arabidopsis* WT and *cnih5* seedlings under +P (250 μM KH_2PO_4) or –P (0 μM KH_2PO_4, three days of starvation) conditions. Error bars represent SE (n = 15–16, pools of seedlings from independent experiments; $^{*}P < 0.05$, $^{**}P < 0.01$; Student's t-test, two-tailed). (C) Expression of *At*PHT1;1/2/3 and *At*PHT1;4 in the root microsomal fractions from 11-day-old *Arabidopsis* WT and *cnih5* seedlings under +P (250 μM KH_2PO_4) or–P (0 μM KH_2PO_4, three days of starvation) conditions. The relative expression level of *At*PHT1;1/2/3 and *At*PHT1;4 was normalized with the corresponding amido black staining and relative to the WT control. Error bars represent SE (n = 2, pools of seedlings from independent experiments). (D) Quantification of Pi uptake and shoot-to-root distribution. Data are visualized using BoxPlotR (Spitzer *et al.*, 2014). The centre lines show the medians; the central plus signs (+) show the means; box limits indicate the 25th and 75th percentiles; whiskers extend to the minimum and the maximum values. Data points are plotted as dots. Data significantly different from WT are indicated by asterisks (n = 8 biological replicates; $^{*}P < 0.05$, $^{**}P < 0.01$; Student's t-test, two-tailed).

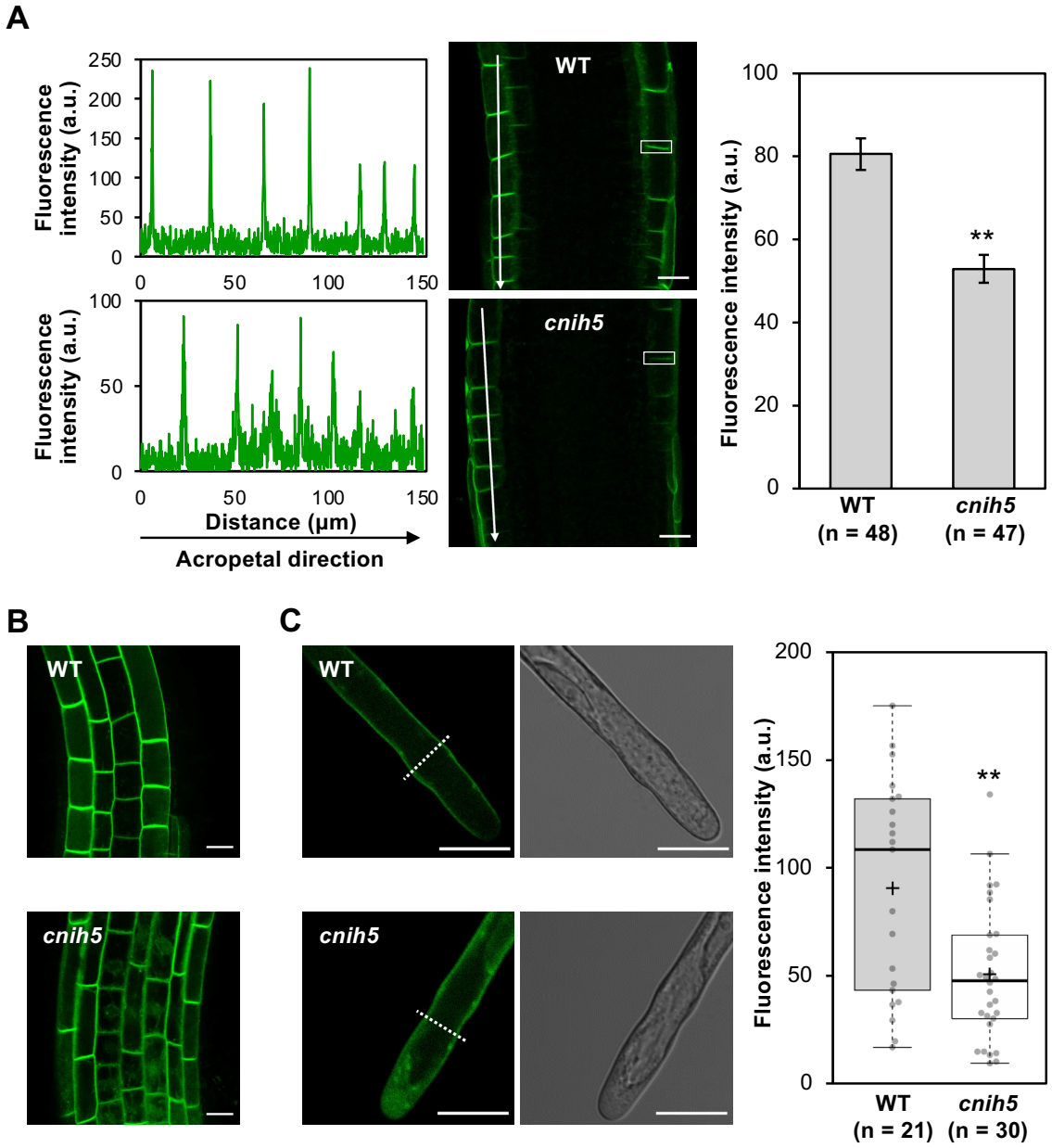

Fig. 5 Impaired plasma membrane targeting of split-GFP-tagged *At*PHT1;1 in *cnih5* root. (A) Reduction of *At*PHT1;1-S11 at the plasma membrane of the epidermal cells in the root transition/elongation zone of 5-day-old *cnih5* seedlings under −P (0 μM KH_2PO_4) conditions. The transgenic lines expressing *AtPHT1;1pro*: *At*PHT1;1-S11/*35S*: GFP1–10 in the *cnih5* and corresponding WT backgrounds were used for comparison. Representative images and line-scan fluorescence intensity profiles (arbitrary unit, a.u.) of *At*PHT1;1-S11 are shown in the left panel. Arrows indicate the acropetal direction. The fluorescence intensity histogram of *At*PHT1;1-S11 enclosed by the representative rectangle is quantified in the right panel. Data significantly different from WT are indicated by asterisks (n, counted regions from transition/elongation zone of 8 roots; $^{**}p < 0.01$; Student's t-test, two-tailed). Scale bars, 20 μm. (B) A representative image shows increased intracellular retention of *At*PHT1;1-S11 in the root epidermal cells along the transition zone and the elongation zone of *cnih5*. Scale bars, 20 μm. (C) Reduction of *At*PHT1;1-S11 at the plasma membrane in the *cnih5* root hair. Line-scan profiles were performed at a distance of 30 μm from the root hair tip as indicated by the dashed line for quantification of PM fluorescence intensity (arbitrary unit, a.u.). All the fluorescence images are acquired from a single confocal optical slice. Quantitative data in the right panel are visualized using BoxPlotR . The centre lines show the medians; the central plus signs (+) show the means; box limits indicate the 25th and 75th percentiles; whiskers extend to the smallest data point within 1.5 times the interquartile range from the lower and upper quartiles. Data significantly different from WT are indicated by asterisks (n, counted root hairs; $^{**}p < 0.01$; Student's t-test, two-tailed). Scale bars, 20 μm.

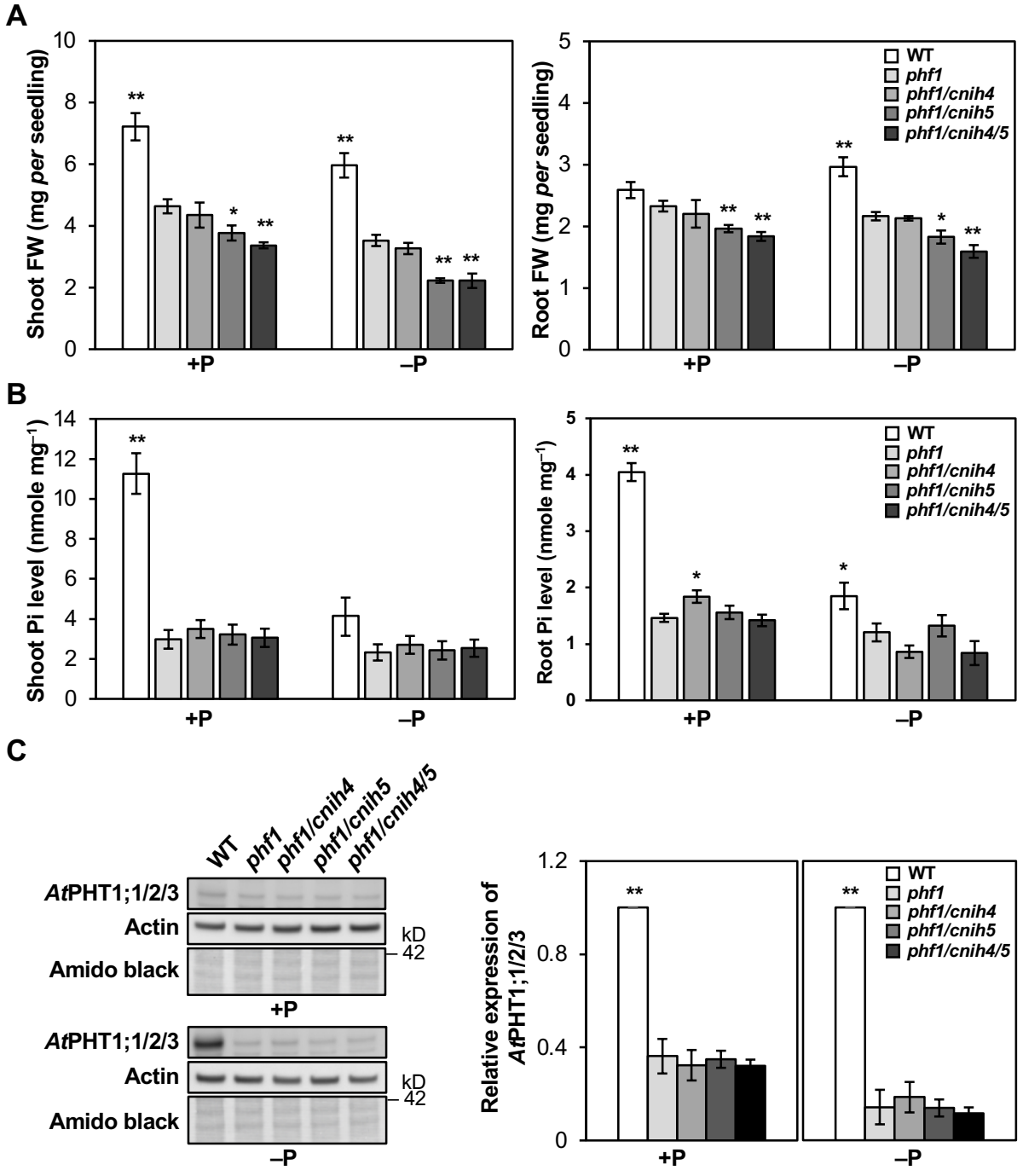

Fig. 6 Loss of *AtCNIH5* exacerbates the growth retardation of *phf1*. (A, B) The shoot and root fresh weight (FW) (A) and Pi levels (B) of 11-day-old *Arabidopsis* WT, *phf1, phf1/cnih4, phf1/cnih5*, and *phf1/cnih4/5* seedlings grown under +P (250 μM KH_2PO_4) or –P (0 μM KH_2PO_4, three days of starvation) conditions. Error bars represent SE (n = 7–8, pools of seedlings from independent experiments). (C) The expression of *At*PHT1;1/2/3 in the root of 11-day-old *Arabidopsis* WT, *phf1, phf1/cnih4, phf1/cnih5*, and *phf1/cnih4/5* seedlings grown under +P (250 μM KH_2PO_4) or –P (0 μM KH_2PO_4, three days of starvation) conditions. The relative expression level of *At*PHT1;1/2/3 was normalized with the corresponding actin and relative to the WT control. Error bars represent SE (n = 3, pools of seedlings from independent experiments). One-way ANOVA with post-hoc Dunnett's test versus *phf1*, $^{*}p < 0.05$, $^{**}p < 0.01$.

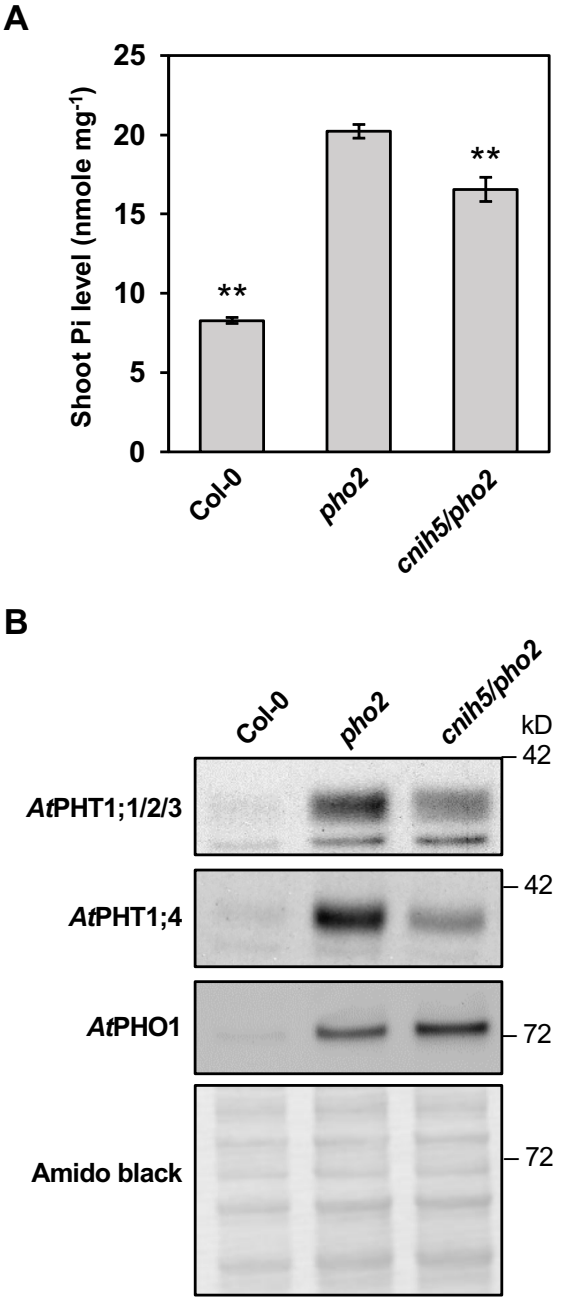

Fig. 7 Loss of *AtCNIH5* suppresses Pi accumulation in *Arabidopsis pho2*. (A, B) The shoot Pi level (A) and the expression of *At*PHT1;1/2/3, *At*PHT1;4, and *At*PHO1 in the root (B) of 11-day-old *Arabidopsis* WT, *pho2,* and *cnih5/pho2* seedlings grown under +P (250 μM KH_2PO_4) conditions. Error bars represent SE (n = 5–7, pools of seedlings from independent experiments). One-way ANOVA with post-hoc Dunnett's test versus *pho2,* $^{**}p < 0.01$. One representative immunoblot from two independent experiments is shown.

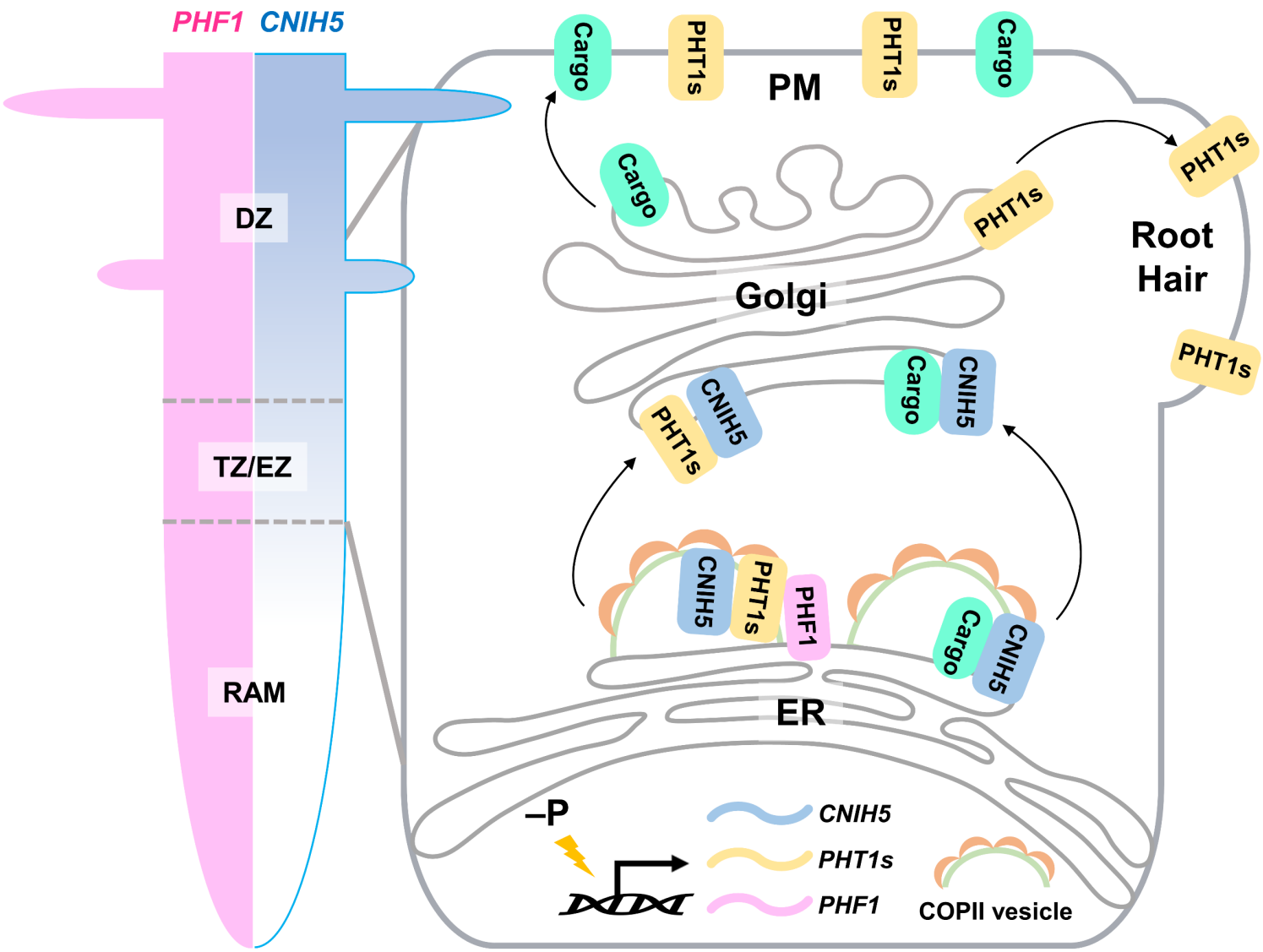

Fig. 8 A working model of *At*CNIH5-mediated ER exit of *At*PHT1s. In *Arabidopsis*, *PHF1* and *CNIH5* are expressed at distinct and overlapping root developmental zones (left panel). In the non-dividing epidermal cell (right panel), including the transition zone/elongation zone and the root hair cell of the differentiation zone, the transcripts of *PHT1* genes, *PHF1*, and *CNIH5* are increased under Pi starvation (−P). CNIH5 interplays with PHF1 to facilitate the ER exit and the plasma membrane (PM) targeting of PHT1s in a COPII-dependent manner. While PHF1 may interact with PHT1s that are competent for the ER exit at an upstream step of COPII recruitment, CNIH5 may selectively mediate the efficient incorporation of PHT1s into the COPII vesicle delivered to the Golgi. CNIH5 may also act as a cargo receptor for other membrane proteins. RAM, root apical meristem; TZ, transition zone; EZ, elongation zone; DZ, differentiation zone.

Table 1. Intracellular retention of split-GFP tagged-*At*PHT1;1 in the root transition/elongation zones of *cnih5*.

			Root 1	Root 2	Root 3	Root 4	Average (%) ± SE (n=4)	*P*-value
			No. of cells with intracellular PHT1;1 /No. of counted cells					
TZ/EZ	Exp. 1	WT	0/9	0/13	5/18	1/12	9.0±6.6	<0.001
		cnih5	10/17	9/15	11/15	8/12	64.7±3.4	
	Exp. 2	WT	1/12	1/13	0/7	0/9	4.0±2.3	<0.001
		cnih5	7/12	4/8	7/9	5/6	67.4±7.9	

- TZ, transition zone; EZ, elongation zone.
- Exp. 1 and Exp. 2 represent two independent experiments. In each experiment, four seedlings expressing *At*PHT1;1-S11 in either the WT or *cnih5* background were used for image analysis.
- Average (%) ± SE (n = 4) indicates the mean percentage of cells containing intracellular *At*PHT1;1-S11 among those counted, along with the standard error of the mean.
- *P*-value is calculated based on a two-tailed Student's t-test.